

Wind Waves

Fabrice Ardhuin¹ and Alejandro Orfila²

¹Univ. Brest, CNRS, IRD, Ifremer, Laboratoire d'Océanographie Physique et Spatiale (LOPS), IUEM, Brest, France ; ²IMEDEA, Esporles, Spain

Wind-generated waves dominate sea surface motions for periods shorter than 300 seconds. Waves are of interest for many applications ranging from navigation safety to ocean and coastal engineering. Waves also define air-sea fluxes and have important interactions with surface currents, upper ocean turbulence, and sea ice. Given the general focus of this book, we emphasize here the successes of wave forecasting methods, starting with a review of basic principles and how wave energy and momentum are modeled. In particular, we discuss the connection between wave modeling and remote sensing, and opportunities for joint measurements of currents and waves. A more detailed account of wave research and applications to geosciences can be found in Ardhuin (2018).

Introduction

Wind waves, which we shall simply call waves in this chapter, are surface waves that derive their energy and momentum from the wind blowing over water. A detailed knowledge of wind fields is thus necessary for the determination of wave properties, which is often sufficient in the sense that we do not need to have wave measurements to make accurate wave forecasts. Still, it is not the local wind that defines the local wave field. Indeed, most of the energy transferred from wind to waves is lost to the upper ocean turbulence by wave breaking. Like any type of wave, wind waves also carry horizontal momentum. For a sine wave, the total wave energy per unit horizontal area E_t is equal to this momentum per unit area M_w times the phase speed C , which is the speed of wave crests. This is a very general relationship that also applies to photons, internal waves, etc. Hence the wind transfers momentum from the wind to the waves, and wave breaking transfers that momentum to surface currents, as illustrated in Fig. 14.1.

Because of this near equilibrium between the wind source and the breaking sink, the wave field grows on time scales of hours to days when the wind is blowing. By definition, the waves that grow due to the local wind form the wind-sea. The degree of development, called the wave age, is measured by the ratio of the phase speed of the dominant waves C_p and the wind speed at 10 m height U_{10} . With room to propagate across ocean basins, waves can persist as swells. Swells do not gain energy from the local wind, on the contrary they lose energy to the atmosphere. Wind-sea due to the local wind and swells generated by remote winds are the two constituents of the sea state.

Ardhuin, F., and A. Orfila, 2018: Wind waves. In "New Frontiers in Operational Oceanography", E. Chassignet, A. Pascual, J. Tintoré, and J. Verron, Eds., GODAE OceanView, 393-422, doi:10.17125/gov2018.ch14.

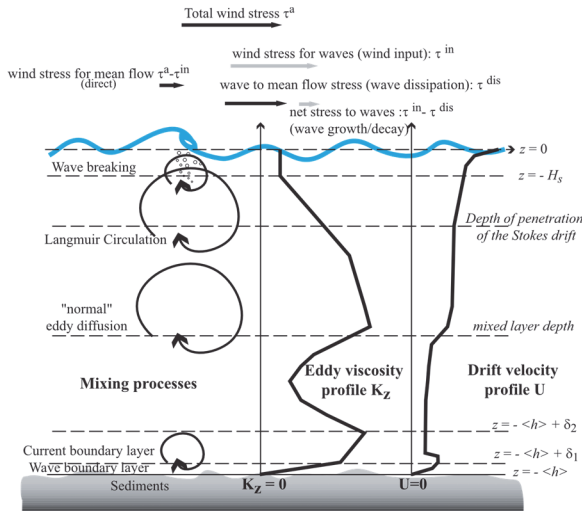


Figure 14.1. Momentum fluxes and mixing processes coupling waves and currents. Processes for horizontally uniform conditions, and possible profiles of eddy viscosity and drift velocity. (From Ardhuin et al., 2005).

A bit of history: 100 years of wave forecasting

After introducing these basic concepts of wind-sea, wave age, and swell, a short tour of wave forecasting history will provide some context. Wave forecasting is a branch of marine meteorology that started soon after the advent of operational weather forecasting in the late 19th century, with a focus on wind storms over the ocean and the associated waves. Driven by the needs of French naval operations around 1910 in Morocco, a first swell forecasting center was established in 1921 in Casablanca (Montagne, 1922) based on a method developed by Gain (1918). The center forecasts used sea level pressure measurements to track storms in the North Atlantic and swell measurements from the Azores to forecast the swells arriving in Morocco. This experience was used in the general wave forecasting method that would be adopted by the Allies for amphibious landings, from Morocco in 1942 to Normandy, and countless Pacific islands in 1944 and 1945. This work is summarized by Sverdrup and Munk (1947) in a report that was declassified after the war. The application and performance of these forecasts are well described by Bates (1949): forecasts for Normandy were good 88% of the time, corresponding to 20% error for heights around 1.5 m. Other war efforts at the UK Admiralty led to great advances on the measurement and analysis of waves, including the introduction of Fourier analysis (Barber et al., 1946). The dispersive nature of swells, with long periods propagating faster, naturally led to the adoption of spectral modeling, in which the surface elevation is represented by a sum of many sinusoidal components with different wavelengths and directions. The first numerical spectral wave model was put into operation by the Casablanca Group (Gelci et al., 1957). An important development of the 1960s was the realization that non-linear wave-wave interactions were a key process in the formation of wind wave spectra, with an inverse cascade of energy towards long period waves. The theoretical work was pioneered by Hasselmann (1962), with experimental verification in a series of experiments known as the Joint North Sea WAve Project (Hasselmann et al., 1973). Today the main physical processes leading to the evolution of wave spectra are usually well identified. In deep water without sea ice they include

wave generation by the wind, non-linear interactions, wave breaking (often called whitecapping in that context), and swell dissipation presumably due to air-sea friction (Ardhuin et al., 2009). Still, the details of these processes are poorly known and involve complex and turbulent motions on both sides of the air-sea interface, such that numerical wave models rely on parameterizations that are still very empirical (e.g. Ardhuin et al., 2010; Stopa et al., 2016).

Expanding applications

Further, new applications and recent investigations have considerably broadened the scope of numerical wave models, leading to extensions towards both longer and shorter wave periods. Although they share most of their kinematic and propagation properties, it is customary to distinguish surface gravity wave categories according to their source of energy, which are indicated in green in Fig. 14.2. The wind waves covered in this chapter are taken broadly, including infragravity (IG) waves and all shorter components; we will discuss waves with periods from 1 second to 5 minutes.

The combination of coastal engineering, remote sensing, and seismology has led to the extension of regional wave models into the long IG range, showing reasonable skill that can be used to interpret future high-resolution satellite altimetry missions and microseismic records (Ardhuin et al., 2014, 2015). These same IG waves are a key component of extreme sea level and nearshore erosion (Reniers et al., 2004), and may play a role in the break-up of ice shelves (Bromirski et al., 2010).

Ocean and coastal engineering: The interest in marine renewable energies, in particular wind power to be recovered from floating platforms, has expanded the existing needs of coastal engineering. These coastal needs were behind many of the early efforts on wave research (e.g., Boussinesq, 1872; de Saint-Venant and Flamant, 1888; Miche, 1944; Iribarren and Nogales, 1949), relayed by offshore engineering when drilling for oil and gas led to many advances in wave dynamics and statistics (Cavanié et al., 1976; Tayfun, 1980).

Remote sensing: Another driver for wave research starting in the 1970s was the booming space age with the cold war in the background. The new capability to measure ocean properties from space, demonstrated in 1972-1973 with Skylab's altimeter and L-band radiometer, meant that ocean wave contributions to remote sensing data required a detailed investigation of the short ocean waves that contribute to the measured signals. Although short wave properties have long been related to wind speed alone (e.g., Cox and Munk, 1954), it is clear that long waves also contribute to the statistics of surface slope (Gourrion et al., 2002). These long waves are not fully determined by the local wind speed. Surface slope statistics can be predicted by the same numerical wave models that are used for marine weather forecasting (Ardhuin et al., 2010). These models still suffer from important errors on the directions of short waves (Peureux and Ardhuin, 2016). Remote sensing applications still largely use the wave spectrum shape of Elfouhaily et al. (1997) defined from three parameters: the wind speed, direction, and the wave age, but its directional distribution does not have the double peak (Peureux et al., 2017) that may be necessary to reproduce L-band observations (Yueh et al., 2013).

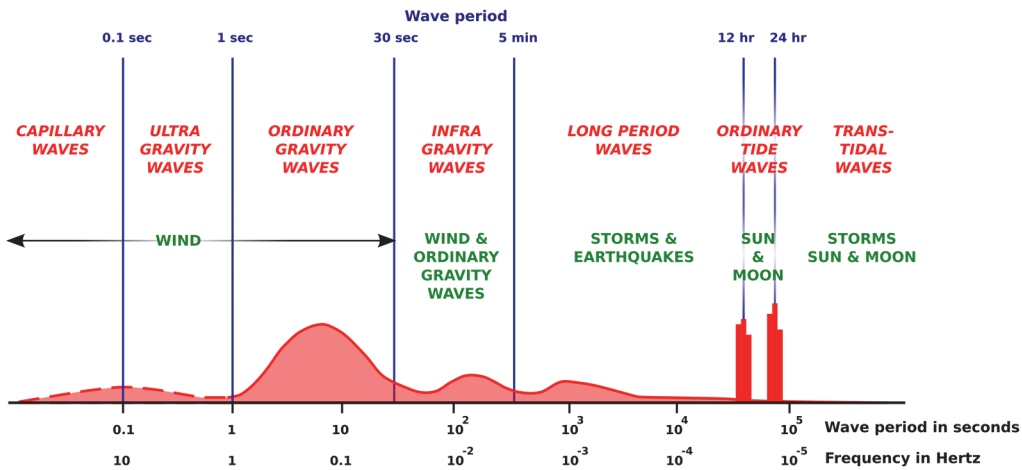


Figure 14.2. Classification of ocean waves according to wave periods. The sources of energy for the various portions of the spectrum are shown in green. The order of magnitude of the relative amplitudes is indicated by the curve (Adapted from Munk, 1950).

Weather and storm surge forecasting: These short waves are also expected to define the surface roughness for the atmospheric boundary layer (Plant, 1982; Janssen, 1989), with a large impact on storm surges (Mastenbroek et al., 1993). Hence, waves have now become an important component in weather forecasting. The ECMWF (European Centre for Medium-Range Weather Forecasts) atmospheric model is coupled to the wave model WAM, operationally since 1998 (Janssen et al., 2001), and in all ECMWF reanalyses. WAM estimates a roughness length that changes the atmospheric boundary layer. The variation of wind stress with wave age was found to modify the intensification of storms and is known to have a strong effect on the life cycle of hurricanes (Jarosz et al., 2007). The actual quantitative variation of wind stress with waves is still the topic of active research with a strong impact on high wind speeds given by atmospheric models: at 30 m/s ECMWF winds and KNMI-processed ASCAT winds are both biased low by 7 m/s compared to other data sources (Pineau-Guillou et al., 2018).

Earth system science (upper ocean and sea ice): Besides atmospheric roughness and wind stress, waves define the flux of turbulent kinetic energy going into the upper ocean, dominated by wave breaking (Agrawal et al., 1992). Another source of turbulence is the stretching by the wave-induced Stokes drift, which is a source of energy for the Langmuir circulation. This circulation consists of roll vortices elongated in the wave direction that are probably the dominant source of mixing in the upper ocean (Kukulka et al., 2009; Sullivan and McWilliams, 2010; D’Asaro, 2014). Waves also contribute to the generation of air bubbles that typically double the air-sea exchange surface and facilitate gas transfer (Deane and Stokes, 2002). On the air side, spray generation is the source of salt aerosols and other atmospheric constituents.

Waves also play a dominant role at the edges of the sea ice and define a Marginal Ice Zone (MIZ) in which air-sea fluxes are enhanced by the wave motion. Ice formation is enhanced by waves via the formation of frazil and pancakes (Shen et al., 2001). Pancake ice, as illustrated on Fig. 14.3, can cover vast regions of the ocean, extending hundreds of kilometers in the Southern Ocean. Waves can also break up the pack ice, sometimes over hundreds of kilometers as well, and in the melting

season it increases lateral melting. Beyond the region of broken ice, waves may propagate with low amplitudes all across the Arctic. The interaction of waves, ice, and the upper ocean is the topic of very active research.

Beyond (upper atmosphere and solid Earth): Finally, wind waves are also the main source of background seismic waves in the solid earth (these are known as microseisms) and acoustic waves in the atmosphere (microbaroms) in particular at periods around 5 s. This background signal can be used to either characterize the noise source (the wind waves) or characterize the medium through which the seismic or acoustic waves propagate. This gives access to the structure of the solid Earth, including time-variations due to volcanic activity, stress changes around faults, etc., and wind speeds in the upper atmosphere at heights of a few tens of kilometers. Fig. 14.4 shows an example of ground motion amplitude (less than 1 micrometer in this case), which is very well explained by the ocean waves activity using the model of Ardhuin et al. (2011).

Seismic measurements such as those shown in Fig. 14.4 have been routinely taken since the 19th century and they contain a climatic record of storm activity (Algué, 1900; Bernard, 1990; Grevemeyer et al., 2000). After pioneering work by Longuet-Higgins (1950) and Hasselmann (1963), we are just beginning to understand the details of the coupling of wind waves with seismo-acoustic waves (Ardhuin et al., 2015), thanks to more accurate wave models and the rapid growth of seismic observation networks. This is still a very exploratory field of research with important applications in seismology (e.g., Shapiro et al., 2005).



Figure 14.3. Picture of pancake ice in the Beaufort Sea taken during the “Sea State” cruise (Rogers et al., 2016). The yellow buoy is a SWIFT wave-measuring drifter with a diameter of 30 cm.

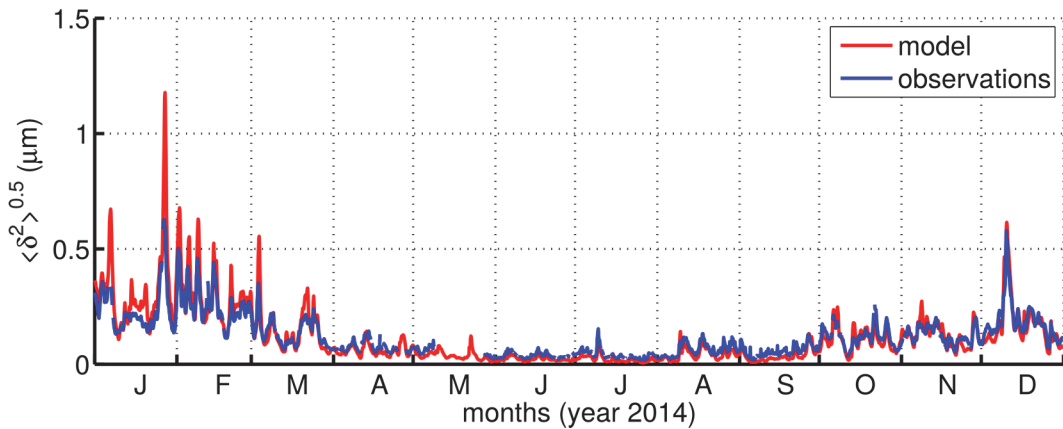


Figure 14.4. Example of measured and modeled time series of vertical ground displacement standard deviation, measured at the Royal Observatory of Uccle in Brussels, Belgium (data courtesy of T. Lecocq). Peaks are associated to storms in the North Atlantic (Ardhuin et al., 2011).

Challenges in numerical wave modeling

A key question in the development of wave models is the understanding of wave growth and dissipation processes and their parameterizations. Nonlinear wave evolution is generally thought to be well understood theoretically and relatively well treated in numerical models, provided that one is ready to pay the computational price. Still, all three aspects (growth, dissipation, and nonlinear propagation) are probably more strongly connected than is generally accepted, even in phase-resolved models. Serious theoretical challenges are also posed by the interaction of waves and currents, especially the effects of vertical current shear and waves with sea ice. New observation techniques are slowly changing our understanding of waves. These include stereo-video (Benetazzo, 2006; Leckler et al., 2015), X-band radars from ships or shore, and remote sensing from space.

This chapter is structured as follows. In the second section, we present the spectral properties of ocean waves. This section also covers a discussion about the fundamentals of numerical ocean wave models. In the third section, we discuss practical issues of phase-averaged wave modeling from the accuracy of the forcing to the choice of parameterizations. In the fourth section, we present phase-resolved modeling and nearshore applications. The fifth section discusses remote sensing of ocean waves and the impact of waves on the remote sensing of other parameters, with a particular focus on current measurements using Doppler techniques.

Ocean Waves and Their Spectral Properties

For most applications, only the statistical properties of ocean waves are of interest. In this case, the waves are referred to as ‘sea state’ and usually described by the power spectral density of the surface elevation. The investigation of the shape and properties of individual waves will not be covered here, but can be found in ocean engineering textbooks (e.g., Boccotti, 2000). The ocean wave spectrum is dominated by surface gravity waves with significant variations in their power over

scales of a few hours, and fast modulations in the form of groups over a few wave periods due to a generally broad spectrum. Other gravity waves that take the form of short transient wave packets, such as tsunamis or ship wakes, will not be discussed here.

Linear wave properties

Waves are generally dominated by irrotational flow, and gravity is the dominant restoring force for most of the wind wave scales. We can ignore surface tension for wavelengths larger than 20 cm. These two properties give a dispersion relation that links the wavenumber k , defined from the wavelength as $k = 2\pi/L$ and radian wave frequency σ defined from the period as $\sigma = 2\pi/T$. For any water depth D , it is (de Laplace, 1776)

$$\sigma^2 = gk \tanh(kD), \quad (1)$$

where g is the gravitational acceleration.

This dispersion relation yields the phase speed $C = \sigma/k$, which is the speed of the crests, and the group speed $C_g = \partial\sigma/\partial k$, which is the speed followed by wave groups and is also the speed at which the energy is propagated. These have two simple limits. When $kD \ll 1$, waves are in deep water, and $\sigma^2 = gk$. This gives $C = gT/(2\pi)$ and $C_g = C/2$. On the contrary, if $kD \gg 1$, waves are in shallow water and $\sigma^2 = gDk^2$. These shallow water waves are hydrostatic and not dispersive, with the same speed \sqrt{gD} for all components. The definition of deep or shallow water is thus given by the ratio of the water depth D and wavelength $2\pi/k$ of the ocean wave.

These speeds are further modified by ocean currents, which introduce a Doppler shift. The apparent radian frequency of the waves in a frame of reference attached to the solid Earth is thus,

$$\omega = \sigma + \mathbf{k} \cdot \mathbf{U}. \quad (2)$$

For the sake of simplicity we shall neglect the vertical variation of the current velocity and take \mathbf{U} to be the horizontal vector of the surface current. In deep water, a 10 s ocean wave has a wavelength of 156 m, a phase speed of 15 m/s and a group speed of 7.5 m/s. Typical swells from a major hurricane have periods around 15 s, and they travel 50% faster, but it still takes them five days to cross the Atlantic from Cape Hatteras to the Bay of Biscay. Longer ocean waves propagate faster, but the upper limit is around 220 m/s for IG periods of 200 s, due to the limited water depth. Indeed, linear waves much longer than the ocean depth propagate at the so-called ‘shallow water’ speed \sqrt{gD} . With a water depth $D = 5000$ m, this speed is 220 m/s.

Typical sea states

Wind waves take all their energy from the wind, more or less directly. The direct transfer only occurs for waves slower than the wind, and the wave-wave interaction flux can push energy up to speeds 20% faster than the wind speed (Pierson and Moskowitz, 1964). As a result, ocean wave periods T are constrained by the dispersion relation (3.1) to be under 30 s for usual ocean waves. For $T = 30$ s, the phase speed C is 47 m/s in deep water, corresponding to the maximum wind speed in a category-2 tropical cyclone. However, this kind of cyclone typically does not generate wave

periods larger than 16 s. This is because the wind speed is necessary, but not sufficient. Indeed, in order to reach large periods and heights, waves need time and space to develop because they grow slowly, on the time scale of days for the highest wind speeds (Hasselmann et al., 1973). The distance over which the waves develop is called fetch. Typical growth behavior of wave heights is shown in Fig. 14.5

Both give the time-limited growth for large fetches and the fetch-limited growth for large durations, with no more growth when waves reach full development at H_s 10.8 m: that value is only a function of wind speed. The dashed line is the same in both panels.

As a result, the waves with largest height and periods are not found in tropical cyclones, which move too fast, but in those extra-tropical storms that travel at the group speed of the dominant waves. For example, the largest ever sea state was measured in such an extra-tropical storm in the North Atlantic, with a maximum significant wave height $H_s = 20.1$ m, and a peak period of 25 s (Hanafin et al., 2012). Thus, ocean wave properties are determined by the space and time patterns of the wind speed and direction, the shoreline geometry, and the water depths. Sea ice also modifies wave propagation and dissipation by impeding the transfer of energy from wind to waves and causing an extra dissipation that is particularly strong for higher frequencies (e.g., Ardhuin et al., 2016). Swells are the waves radiated away from storms, with typically longer periods than wind sea because shorter components dissipate rapidly in the absence of wind forcing. Near the shoreline, these wind-generated waves can interact non-linearly to produce longer ocean wave periods, up to 300 s. Those long waves are called IG waves (Munk, 1950; Longuet-Higgins and Stewart, 1962). Some examples of ocean wave spectra are shown in Fig. 14.6 and discussed in the next section.

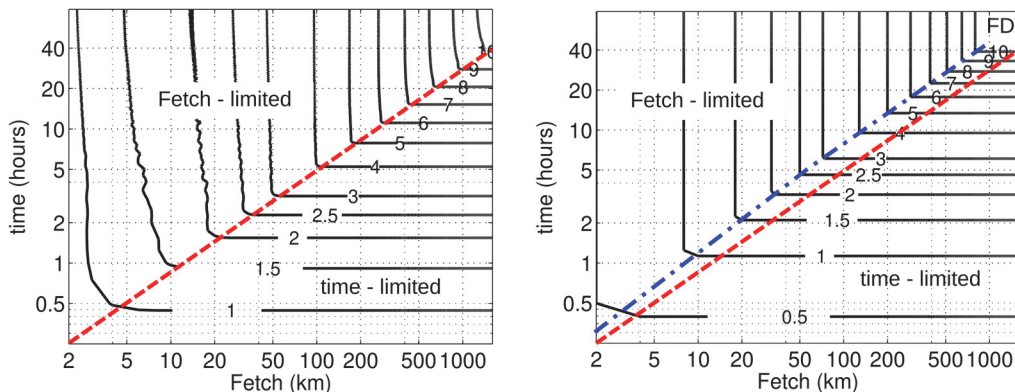


Figure 14.5. Estimation of significant wave height (H_s , contours) as a function of fetch and time for the idealized case of an infinitely long coast with a wind blowing perpendicularly offshore at a speed $U_{10} = 20$ m/s. In the left panel, the estimate is given by a numerical integration of the wave energy or action equation (3), using parametrizations for the wind-wave growth and dissipation from Rascle and Ardhuin (2013) and non-linear wave-wave interactions from Hasselmann et al. (1985) in the WAVEWATCH III model, with a third order numerical scheme Tolman (1995). The right panel combines empirical growth curves (Elfouhaily et al., 1997).

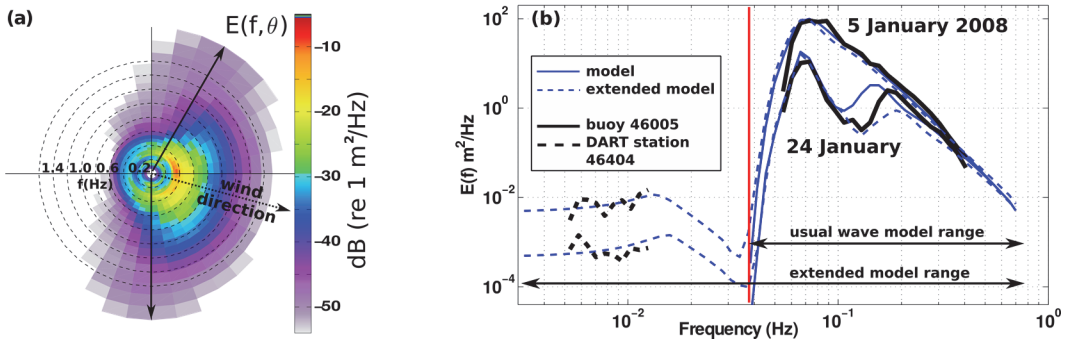


Figure 14.6. (a). Example of directional wave spectrum $E(f, \theta)$ as a function of azimuth θ and frequency f as recorded by a stereo video system in the Black Sea (Leckler et al., 2015). The high frequency of the peak, f_p 0.33 Hz, is typical of small seas or weak winds, but the directional shape of the spectrum is expected to be similar to that found in the open ocean for similar values of f/f_p . At relative high frequencies ($f/f_p > 3$) the dominant directions (solid arrows) can be 70° away from the wind direction (dashed arrow). (b) Example of modeled and measured wave spectra $E(f)$ in the North-East Pacific, on 5 (top curves) and 24 (bottom curves) January 2008. Classical wave models provide wave spectra between 0.04 and 0.7 Hz (blue solid line). Ardhuin et al. (2014) have extended that range to include infragravity (IG) waves down to $f = 3 \times 10^{-3}$ Hz (blue dashed line).

Numerical wave modeling

Numerical ocean wave models were first developed for navigation safety (Gelci et al., 1957) and are generally based on an evolution equation for the wave spectrum. At each point of the ocean surface, the sea state is represented by a two-dimensional power spectral density $E(f, \theta)$ that gives the distribution of surface elevation variance across frequencies f and directions θ . Wave energy propagates in all directions θ at the speed given by the group velocity C_g that is a function of frequency f . In deep water, $C_g = g/(4\pi f)$ is half of the phase speed, hence $C_g = 8$ m/s at $f = 0.1$ Hz. For a flat ocean bottom, the evolution of the power spectral density, $E(f, \theta)$, is given by

$$\partial E(f, \theta) / \partial t + \text{propagation at speed } C_g = S(f, \theta), \quad (3)$$

where the left side represents wave propagation, and the right side source term S represents many processes including generation by the wind (e.g., Janssen, 2004), non-linear wave evolution (Hasselmann, 1962) and dissipation by wave breaking or wave-ice interactions (Ardhuin et al., 2010, 2016).

Both E and S vary with the horizontal coordinates x and y , as well as with frequency f and azimuth θ . For each frequency and direction, the source term $S(f, \theta)$ is also a function of the spectral density $E(f, \theta)$ evaluated at all the other frequencies f and directions θ , but at the same location given by x and y . The source term S is also a function of many other parameters including wind speed and direction, water depth, ice and ocean bottom properties. In practice, there is no expression for S that is based on first principles, and empirical parameterizations are the topic of ongoing research (e.g., Ardhuin et al., 2010).

There are very few measurements of the full two-dimensional ocean wave power spectral density as a function of azimuth θ and frequency f , such as the one shown in Fig. 14.6.a. Numerical

wave models have been calibrated and validated mostly in terms of dominant ocean wave frequency f_p , and significant wave height H_s , defined as

$$H_s = 4\sqrt{\int E(f)df} \quad \text{with} \quad E(f) = \int E(f, \theta)d\theta \quad (4)$$

Most wave measurements done in situ rely on time series of pressure, velocity, and/or surface elevation, so that it is usual to work with the one-dimensional power spectral density of the surface elevation $E(f)$. A typical frequency range of measurements and models goes from a minimum around 0.03 Hz to a maximum somewhat below 1 Hz. It is fairly common to have a good estimate of H_s but a not-so-good spectral distribution $E(f)$. Fig. 14.6.b shows measured spectra and results of a numerical ocean wave model (The WAVEWATCH III^(R) Development Group, 2016) off the Oregon coast, where the water depth is 4000 m, on 5 and 24 January, 2008. The extended modeled and measured spectra are for the location of the tsunameter DART 46404 system, 200 km to the east of the wave buoy 46005. On 5 January, the model reproduces well the single peak at 0.07 Hz. On 24 January, the swell peak at 0.07 Hz is relatively well modeled, while the peak of the wind sea is at 0.15 Hz in the model and 0.18 Hz in the buoy data due to errors in the wind speed used to drive the wave model. As a result there is a large difference in the energy level at 0.15 Hz. These results depend mostly on the accuracy of winds used to force the wave model.

Operational Wave Hindcasting and Forecasting

Global to regional scales

At the scale of ocean basins, the most common models solve a wave energy equation similar to Eq. 3—usually with the addition of refraction—on regular grids in latitude and longitude (Janssen, 2008) or on multiple-grid systems that allow refinement close to shore (Tolman, 2008) where the sea state is impacted by shoreline geometry. The specific implementations depend on the sea state encountered in different regions. In particular, the frequency range over the open ocean should extend below 0.04 Hz to reproduce the rare but very strong storms (e.g., Hanafin et al., 2012). This is not necessary for a model restricted to an enclosed basin such as the Mediterranean, where long waves have no room to develop. High spatial resolution is also preferred for hurricane modeling, and moving or adaptive grids have been tested in research but, to our knowledge, are not used now in operational forecasting system.

The accuracy of wave models has benefitted from steady improvements in the accuracy of winds, in particular thanks to the assimilation of surface winds (Hersbach, 2010). For forecast ranges of a few days, the model accuracy also benefits from the assimilation of altimeter (Lionello et al. 1992) and synthetic aperture radar (SAR) wave mode data (Lefevre and Aouf, 2012; Hasselmann et al., 2012). In particular, SAR provides a measure of the wave spectrum that has a more lasting impact in the forecasts because it allows to correct initial value errors of the different wave components. The quality of the forecasts is routinely verified using moored buoys (Bidlot et al., 2007; Bidlot, 2017). The accuracy of the wind is the dominant factor for the accuracy of wave forecasts and hindcasts, followed by the effect of parameterizations, and finally a benefit from

assimilation for forecasts ranges of three days or less. Given the importance of the wind forcing, it is no surprise that relatively coarse atmospheric models, such as the ERA-Interim reanalysis, produce low biases on wave heights, and generally wave models have to be tuned to specific wind forcing (Stopa, 2018).

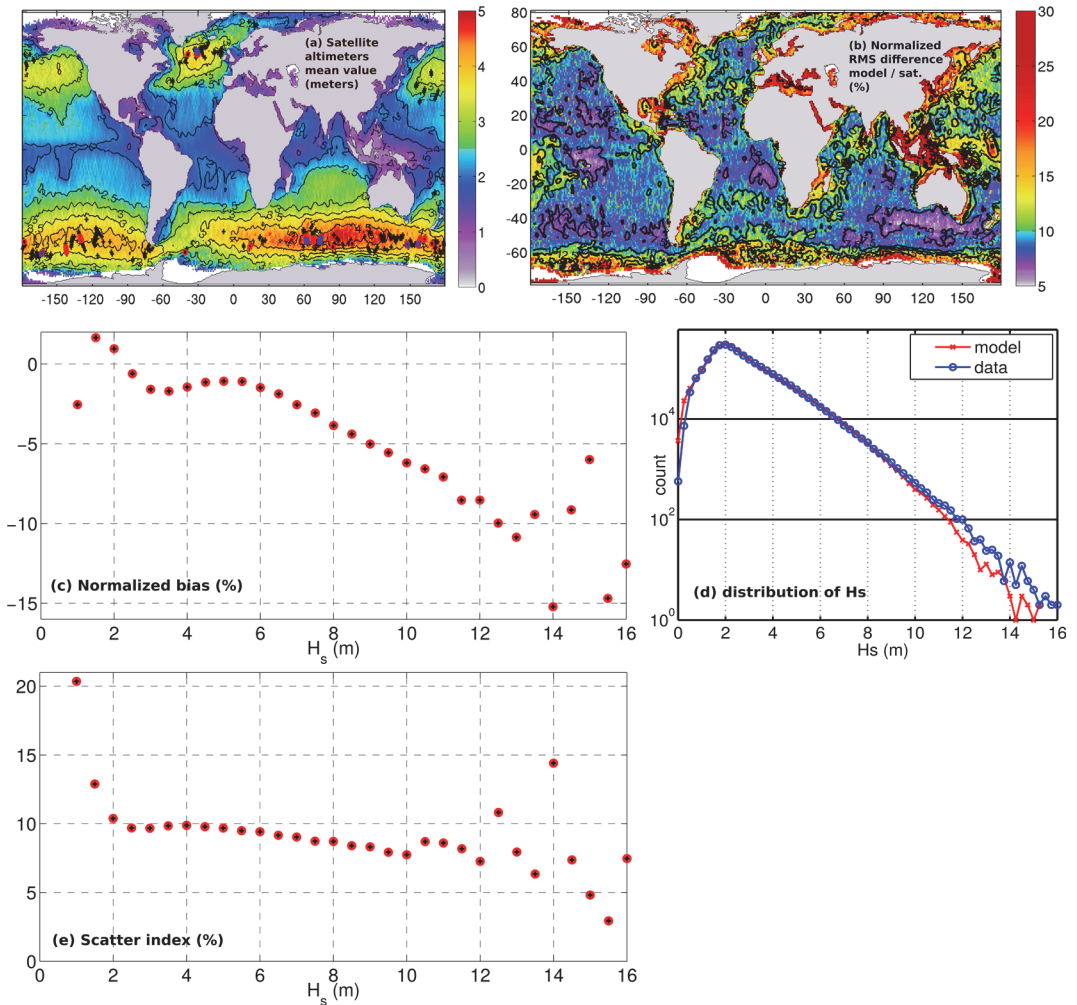


Figure 14.7. The satellite data are along-track averages over 1 degree in latitude, and statistics are based on these “super-observations”, with a total of nearly 3 million super-observations and associated model matchups. (a) Mean value of H_s for the year 2015, as recorded by Jason-2, Cryosat and SARAL-Altika. ‘+’ marks the location of values above 12 m, red ‘o’ are above 14 m and blue squares are above 15 m. (b) Normalized RMS difference between model and altimeter for the year 2015, in percent. (c) Bias (model - satellite) as a function of H_s for the same year, (d) distribution of H_s in co-located model and satellite data and (e), scatter index.

Fig. 14.7.a shows the mean value of H_s in 2015, which does not vary too much from year to year. Although the largest mean values are in the Southern Ocean, the most extreme values of H_s are usually found between Iceland and Ireland. Also, it is interesting to note that extremes in the tropics are dominated by tropical storms. These give lower maximum values of H_s than the largest

extra-tropical storms, because the very high winds are concentrated in the small region around the eye. Still, these extreme H_s in tropical storms are relatively high compared to the annual mean.

For all these extremes, the sampling of satellite altimeters is insufficient, even with three nadir satellite missions.

With altimeter data averaged over 120 km along-track, this average, open ocean wave heights are very accurate with typical errors under 10% of the averaged measured value. The modeled values are produced by the Laboratoire d'Océanographie Physique et Spatiale for various geophysical applications (Rascle and Ardhuin, 2013) and available at <ftp://ftp.ifremer.fr/ifremer/ww3/HINDCAST/>. The model results in Fig. 14.7 do not include current effects, which certainly contribute to the errors off South Africa. Other regions of large errors are in some coastal areas, especially on the west side of ocean basins, and where sea ice is important. The relative large difference between model and altimeter around Indonesia may be largely due to altimeter errors. Indeed, that region has average wave heights under 1 m, for which the altimeters with a typical vertical resolution of 0.4 m are not accurate enough (e.g., Sepulveda et al., 2015).

Predicting low to average wave heights can be important for delicate operations at sea (towing of large structures, maintenance), but very high wave heights and very large periods generally receive more attention. Fig. 14.7.e shows that the highest waves are indeed the most accurately predicted with typical random errors under 8% for $H_s > 12$ m, once the bias has been corrected. This bias is not completely understood but probably comes in part from an underestimation of high wind speeds in the ECMWF model (Pineau-Guillou et al., 2018). Other sources of errors are inappropriate parameterization for wind-wave interactions at very high winds where spray, bubbles, and hydrodynamic instabilities can be important (Soloviev et al., 2014).

At regional to ocean basin scales, the main differences between different wave models come first from the wind forcing, and second from parameterizations of the source term S on the right side of Eq. 3. To a lesser extent, differences can also come from numerical schemes (Ardhuin, 2018, chapter 8).

Effects of depth and currents on waves

The dispersion relation Eq. 1 is modified by surface currents \mathbf{U} into Eq. 2. As a result, the phase speed is also Doppler shifted, and the phase speed of linear waves is a function of wavelength, depth, and current vector. Thus, current gradients are the cause of refraction of waves, just like changes in the water depth. A simple way to understand this effect is to consider wave rays, the trajectories followed by wave crests. Things are simpler for monochromatic waves in stationary conditions and without any dissipation nor diffraction. In the absence of current, the wave energy is conserved and the flux of energy between two rays is constant, where the rays converge with a distance l the energy flux is proportional to $1/l$ and the wave height is proportional to $1/\sqrt{(C_g l)}$.

In the presence of current, the wave energy is not conserved because waves and current exchange energy. This change of wave energy can be interpreted as the work of 'radiation stresses' (Phillips, 1977; Ardhuin, 2018). Still, in the absence of dissipation the wave action $\int E(f, \theta) / \sigma df d\theta$

is conserved. As a result, a similar ray tracing can be performed, with the ray trajectories modified by the current, and the energy flux $C_g E$ replaced by $(C_g + \mathbf{k} \cdot \mathbf{U}/k)E/\sigma$.

In many coastal regions, the significant wave height has a strong tidal modulation, which is due to currents. This modulation is mostly caused by refraction. In the case shown in Fig. 14.8, the typical curvature radius of the rays in the current jet located south-west of the island of Ouessant is around 10 km, as materialized by the green circle. This jet peaks 1.5 hours after the low tide and deviates the waves away from the Pierres Noires buoy, located 20 km down-wave.

Similar effects explain the formation of large waves in the Agulhas current (Lavrenov, 2003), the Gulf Stream or other regions. The variability of wave heights follows that of the surface current and increases when the current gradient in the direction of the wave crests is coherent over long distances (White and Fornberg, 1998). As a result, mesoscale and submesoscale currents induce significant variations in wave heights, as shown in Fig. 14.9

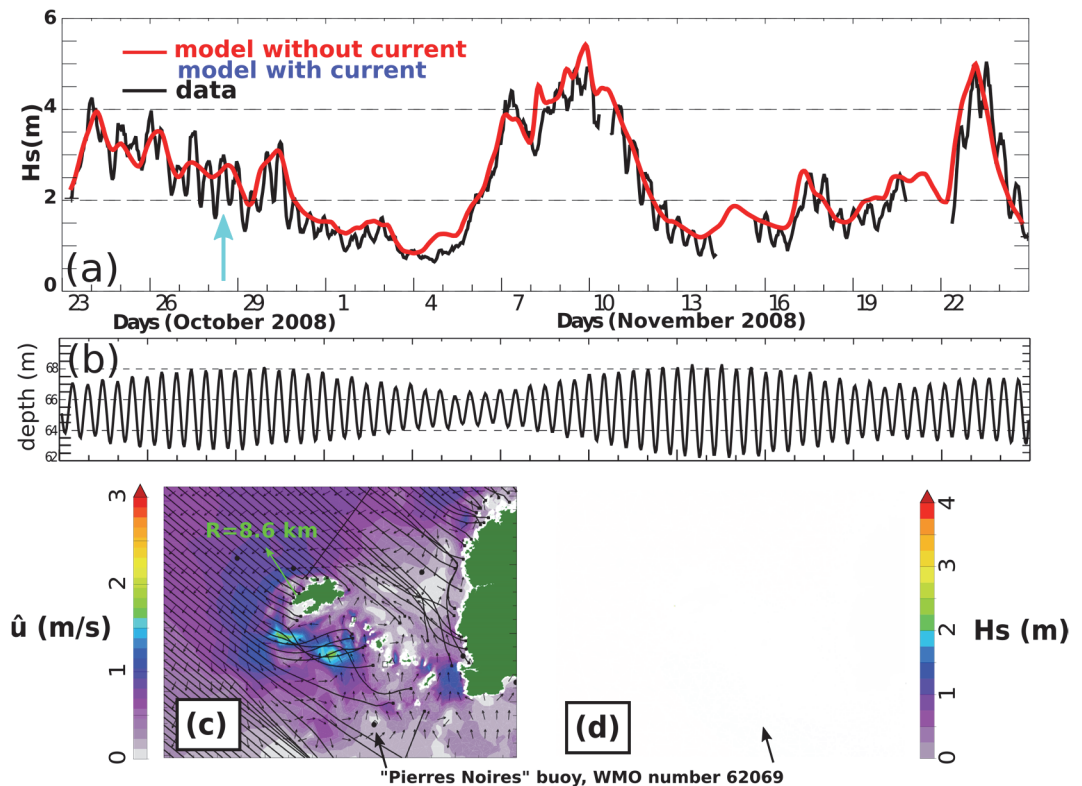


Figure 14.8. Example of strong impact of currents on wave heights due to wave refraction by currents. The top panel shows a time series of H_s recorded at the wave buoy ‘Pierres Noires’ (WMO number 62069) and modeled with WAVEWATCH III, while the middle panel shows the water depth at the buoy. (c) Modeled tidal current and the corresponding wave rays for $T = 10$ s (d) shows H_s and mean wave directions, both for October 28, 2008, at 11:00 AM UTC (corresponding to blue arrow in a). (Adapted from Ardhuin et al., 2012).

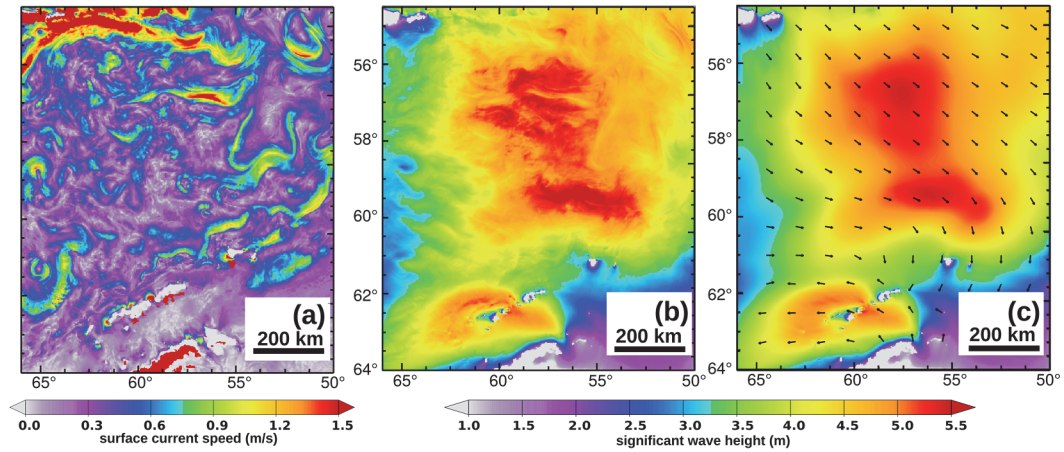


Figure 14.9. Example of (a) surface current magnitude modeled by MITgcm, courtesy of D. Menemenlis, (b) the modeled significant wave height when the current forcing is included (arrows) and (c) modeled significant wave height without effects of currents. (Adapted from Arduin et al., 2017b).

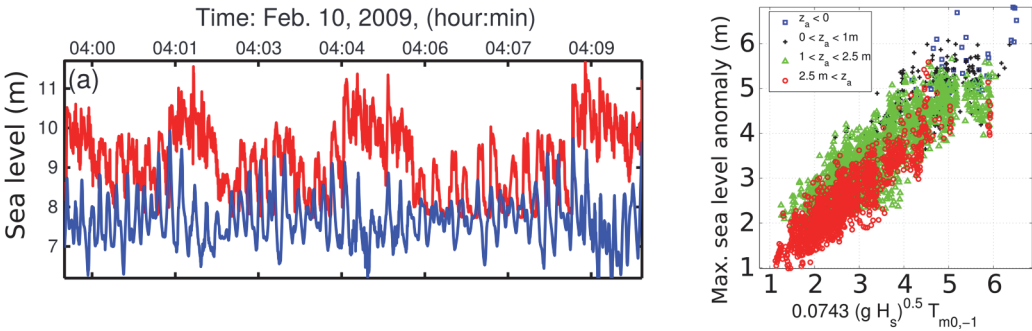


Figure 14.10. Left: example of surface elevation estimated from bottom pressure sensors, recorded on 10 February 2009 04:00:10 UTC at the bottom (blue) and top (red) of a cliff, on the island of Bannec, France. Right: maximum sea level anomaly (sea level minus predicted tide and inverse barometer), at the top of the cliff, as a function of modeled wave height H_s and mean period $T_{m0,-1}$ offshore of the cliff during the winter 2008-2009.

Waves at the coast

We have shown all results for wave heights, but wave periods are also very important for many applications, in particular for extreme water levels at the coast. Indeed, the amplitude of IG waves generated in shallow water is usually related to the presence of long wave groups, which occur when the wave spectrum is narrow. This is most often associated with long wave periods. Fig. 14.10 shows an example of a measured time series of sea level right at the shoreline (Sheremet et al., 2014). These contain very large IG waves with a height exceeding 2 m and a typical period of 300 s. These IG waves contribute to the maximum sea level anomalies and scale with the Hunt parameter defined as $H_H = \sqrt{(g H_s) T_{m0,-1}}$, in which the mean wave period $T_{m0,-1}$ is actually more important than the wave height. Mean periods, are generally defined from the spectrum as

$$T_{m0,n} = [\int f^n E(f) df / \int E(f) df]^{1/n}. \tag{5}$$

In the case $n = -1$, the mean period is also called the energy period because it corresponds to the proper frequency weighting of the energy flux. In practice, H_H and IG wave amplitudes are highly correlated (e.g., Stockdon et al., 2006), which makes possible the definition of an empirical source of IG waves at the shoreline (Fig. 14.11).

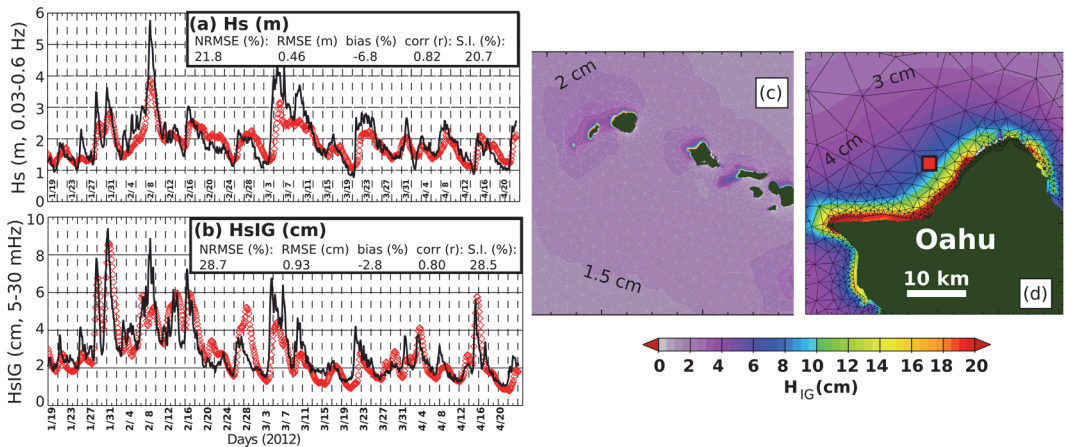


Figure 14.11. Measured (solid lines) and modelled (symbols) wave parameters for Waimea, Hawaii: (a) wave heights, (b) infragravity (IG) wave heights - the dates are written below panel (b) every four days only, starting on January 19, 2012, (c) snapshot of modelled H_{IG} around all the islands, and (d) close-up in the Oahu north shore, where the Waimea buoy and mooring were located (red square), January 31, 2012 at 0 UTC.

Nearshore Dynamics

Given the complexity of wave evolution and the high stakes of beach or harbor management, many different approaches have been developed for dealing with the region of the ocean along the coast that is dominated by intense wave breaking, which we call the nearshore. Phase-averaged models, the same as those at larger scales such as WAVEWATCH III, are still largely used but they fail to reproduce correctly critical aspects of the nonlinear wave evolution in shallow water. Their extension with the bi-spectrum (Herbers and Burton, 1997) is an interesting alternative, but it has been only used for research, probably because users are more familiar with time series of velocities than just their statistical properties (e.g., skewness and asymmetry). Many applications use phase-resolving models, which basically solve the deterministic time dependent mass and momentum balance equations and generally can also model currents at the same time.

It is accepted that shallow water conditions correspond to $kD < 0.3$, with $k=2\pi/\lambda$ the wave number and λ the wavelength, while $kD > 3$ corresponds to deep waters (Dingemans, 1997). In intermediate waters (namely $0.3 < kD < 3$), non linearity and dispersion coexist and neither Airy theory, nor nonlinear shallow water equations can represent properly the physics of wave propagation. To overcome this problem, two main perturbation approaches are found. On the one hand, Stokes theory departs from the fully dispersive linear Airy theory to incorporate weakly nonlinear effects. On the other, Boussinesq-Type Equations (BTEs) depart from nonlinear shallow water equations and include weakly dispersive effects.

In this section, we reviewed some of the theories that have been developed for wave transformation from intermediate waters to the shore. The reader is referred for a more complete overview to Mei (1989), Dingemans (1997), and Liu and Losada (2002).

Depth integrated models

For small amplitude waves, and assuming irrotational motion and incompressibility of water, a velocity potential $\nabla\Phi = u$ exists satisfying the continuity equation, i.e.,

$$\nabla^2\Phi = 0 \quad -h < z < \eta \quad (6)$$

and $D = h + \eta$, the time averaged water depth. This can be solved after defining the conditions at the fixed boundaries (surface and bottom). At the surface, $z=\eta(x,y)$ two conditions have to be specified, the dynamic and the kinematic which establish continuity of stresses at the surface and that the surface is a material interface. At the bottom, $-h(x,y)$, the no-flux condition ensures the bottom as a material surface. The solution for the water wave problem represented by a linear wave $\eta(x,y,t) = a \cos(kx - \sigma t)$ with wave number k and frequency σ propagating over a flat bottom Eq. 6, subjected to the boundary conditions gives for the velocity potential,

$$\Phi = \frac{ag}{\sigma} \frac{\cosh(k(h+z))}{\cosh(kD)} \cos(kx) \sin(\sigma t) \quad (7)$$

where a is the wave amplitude and where wave frequency is related with the wave number through the dispersion relationship (Eq. 1), obtained by combining the two free boundary conditions at the surface.

As the water waves propagate to the coast, the water depth D decreases and the wave propagation becomes influenced by it. Also, nonlinear effects become important. In shallow waters, where the water depth dominates the wave propagation, the wave celerity is given by $C \approx \sqrt{gD}$, which is independent of the wave period (i.e., non-dispersive). An important physical property of shallow waters is that the horizontal velocity profile is nearly uniform in the vertical, nonlinear shallow water equations, which are vertically integrated, exploit this property and are valid for non-dispersive conditions and for arbitrary amplitudes of the wave.

Phase-resolving models need to solve the wavelength with enough resolution, which implies around 20-30 points per wavelength (10-100 time steps per wave period). By contrast, phase-averaged models only need to resolve gradients of the wave amplitude, which is generally less demanding. When a train of monochromatic waves enters a zone of slowly varying bathymetry wavelength changes and the spacing between equal phase lines also changes as the result of the adjust of the phase velocity. Phase-resolving models are still enormously expensive being still limited to specific applications or to the study of processes. The main effort in this subject has been devoted in the development of new theories that reduce the computational cost of the numerical models as well as in the development of a theory able to study the propagation of waves from deep to shallow waters including all the physics of the wave transformation phenomenon (all dispersion ranges).

Early modeling efforts for the transformation of waves from the ocean to the coast traced rays tangent to the wave number vector computing the variation of the wave envelope using the conservation of energy. However, the main problem of ray theory is that it is only valid for small amplitude waves and does not allow diffraction effects. To overcome this limitation, Eckart (1952) first and independently Berkhoff (1972) developed the mild slope equation. The main assumption is that the evanescent modes can be neglected for waves propagating over slowly varying bathymetries, i.e., $\frac{\nabla D}{kD} \ll 1$, except around obstacles. For a monochromatic wave with surface displacement η and frequency σ , Smith and Sprinks (1975) showed that to the leading order the free surface displacement satisfy,

$$\nabla \cdot (C C_g \nabla \eta) + \frac{\sigma^2}{g} \eta = 0 \quad (8)$$

where we recall that $C = \sigma / k$ is the phase velocity and

$$C_g = \frac{\partial \sigma}{\partial k} = C \left(\frac{1}{2} + \frac{kD}{\sinh(2kD)} \right) \quad (9)$$

is the group velocity. The mild slope is suitable to propagate linear waves from deep to shallow water, reproducing correctly the velocity profile according to the linear wave theory.

The main problem of the mild slope equation is to specify the boundary at the coast. Tsay and Liu (1982) and Kirby and Dalrymple (1983) solved this problem by developing the parabolic approximation, which is suitable for waves propagating mainly in one direction. In this theory, wave energy is allowed to diffuse across wave ray including approximately the effects of diffraction. For a free surface displacement $\eta = \psi(x, y) e^{ik_0 x}$ being k_0 a reference wave number and assuming that the wave amplitude varies much slower in the wave propagation direction, and defining $K = C C_g$, Eq. 8 after adopting the parabolic approximation can be expressed as,

$$\frac{\partial^2 \psi}{\partial y^2} + \left(2ik_0 + \frac{1}{K} \frac{\partial K}{\partial x} \right) \frac{\partial \psi}{\partial x} + \frac{1}{K} \frac{\partial K}{\partial y} \frac{\partial \psi}{\partial y} + \left(\frac{\omega^2}{g} - k_0^2 + \frac{ik_0}{K} \frac{\partial K}{\partial x} \right) \psi = 0 \quad (10)$$

The mild slope equation and its parabolic approximation are obtained for linear waves, and the superposition of different frequency components can be made. These models are used extensively for coastal applications since accurate propagation over two-dimensional bathymetries can be modeled with relatively low computational cost.

Boussinesq approximation

There is an intermediate zone where $H/D \ll 1$ and $kD \ll 1$. The Boussinesq Equations (BEs) were developed to represent water wave propagation in this region. BEs can be seen as an extension of the shallow water equations that includes dispersion in a perturbative way. BEs were obtained by Peregrine (1967) for weakly dispersive and weakly non-linear conditions. The extension to weakly dispersive but arbitrary (or fully) non-linear conditions are very popular nowadays (Green and Naghdi, 1976; Wei and Kirby, 1995; Madsen and Schaffer, 1998), and are usually referred to as Serre's Equations, after Serre (1953), or also as Boussinesq-type Equations (BTEs).

BEs and BTEs have ensured a good performance under weakly dispersive conditions (BEs for weakly non-linear conditions and BTEs for arbitrary non-linear conditions), by construction. In order to assess the performance under stronger dispersive conditions, BEs and BTEs are linearized

and compared to linear and fully dispersive theories such as Airy and Mild Slope Equations (Dean and Dalrymple, 1984). The comparison is made in terms of wave celerity (linear dispersion) and wave shoaling over mild slopes (linear shoaling). The weakly non-linear performance is also usually compared to the second order Stokes theory for flat beds (Schaffer, 1996). Since BEs and their corresponding BTEs are identical in their linear weakly dispersive terms, the comparisons give the same results using the BEs or their corresponding fully non-linear extensions (BTEs).

The standard BEs for variable depth expressed in terms of the depth averaged velocity vector \bar{u} are obtained from the conservation of momentum and mass equations by a perturbative approach as,

$$\begin{aligned} \frac{\partial \eta}{\partial t} + \nabla \cdot [(\eta + h)\bar{u}] &= 0 \\ \frac{\partial \bar{u}}{\partial t} + \frac{1}{2} \nabla \bar{u}^2 + g \nabla \eta + \left\{ \frac{h^2}{6} \nabla \left(\nabla \cdot \frac{\partial \bar{u}}{\partial t} \right) - \frac{h}{2} \nabla \left(\nabla \cdot \left(h \frac{\partial \bar{u}}{\partial t} \right) \right) \right\} &= 0 \end{aligned} \quad (11)$$

which can be further coupled with the bottom boundary layer to analyze viscous damping and sediment transport processes (Liu and Orfila, 2004; Orfila et al., 2007).

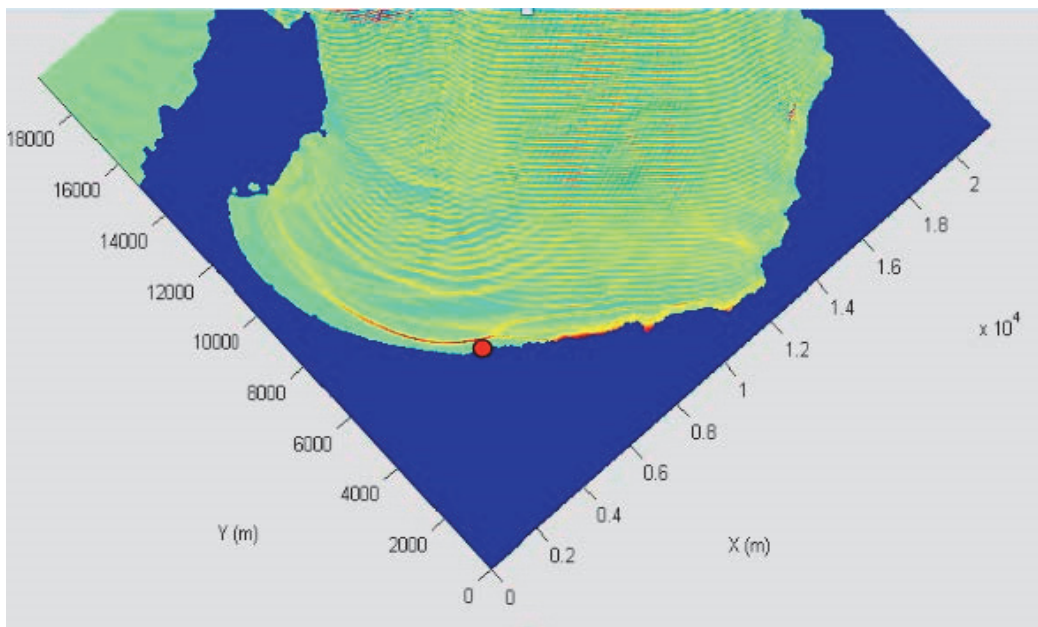


Figure 14.12. Snapshot of free surface elevation in Alcudia Bay (North of Mallorca Island). The computational domain is 20 x 18 km with a fixed grid of 1 m in order to solve the smallest wave lengths.

Although providing very accurate results compared with field and laboratory data (Liu et al., 2006), are still restricted to a small zone since it is required that both nonlinearity and frequency dispersion remain weak. Much of the research in this area during the last 20 years has been devoted to improve the linear properties of the equations. Leaving aside higher order (in dispersive terms) equations (Gobbi et al., 2000), which include spatial derivatives of order five, two main different approaches can be distinguished to this end: i) Madsen and Sorensen (1992) proposed an enhancement technique so as to introduce new terms that improve the dispersive performance, and Beji and Nadaoka (1992) proposed an alternative set of enhanced equations; and ii) Nwogu (1993)

introduced a new set of BEs written for the velocity at $z_\alpha = ah$ (instead of the depth averaged velocity), and chose $\alpha = -0.53096$ to improve the linear dispersion up to $kh \sim 3$. The corresponding depth integrated and continuity equations expressed in terms of the free surface displacement η and the horizontal velocity u_α at the water depth $z=z_\alpha$ are:

$$\begin{aligned} \frac{\partial \eta}{\partial t} + \nabla \cdot [(\eta + h)u_\alpha] + \nabla \cdot \left\{ \left(\frac{z_\alpha^2}{2} - \frac{h^2}{6} \right) h \nabla \nabla \cdot u_\alpha + \left(z_\alpha + \frac{h}{2} \right) h \nabla (\nabla \cdot hu_\alpha) \right\} = 0 \\ \frac{\partial u_\alpha}{\partial t} + \frac{1}{2} \nabla |u_\alpha|^2 + g \nabla \eta + z_\alpha \left\{ \frac{1}{2} z_\alpha \nabla \left(\nabla \cdot \frac{\partial u_\alpha}{\partial t} \right) + \nabla \left(\nabla \cdot \left(h \frac{\partial u_\alpha}{\partial t} \right) \right) \right\} = 0 \end{aligned} \quad (12)$$

The optimal choice of $z_\alpha = 0.53h$ allows to simulate with a good accuracy wave propagation from intermediate water depth to shallow water including wave current interaction as shown in Fig. 14.12.

High order models

In the last 15 years, there has been an intense research work to further extend the range of applicability of BTEs. These models introduce higher order terms or more variables (Agnon, 1999; Gobbi et al., 2000; Lynett and Liu, 2002) and, pushed to their limits, some of them can represent highly dispersive and highly nonlinear waves. As a counterpart, since they contain either more equations or higher order derivatives in the governing equations, they are more demanding with respect to the computational resources compared to low order original models. This makes BTEs such as the above presented widely used nowadays. The highly nonlinear and weakly dispersive wave equations take the form

$$\begin{aligned} \frac{\partial \eta}{\partial t} + \nabla \cdot \left\{ (h + \eta) \left[u_\alpha + \left(z_\alpha + \frac{1}{2}(h - \eta) \right) \nabla (\nabla \cdot (hu_\alpha)) + \left(\frac{1}{2} z_\alpha^2 - \frac{1}{6}(h^2 - h\eta + \eta^2) \right) \nabla \nabla \cdot u_\alpha \right] \right\} = 0 \quad (13) \\ \frac{\partial u_\alpha}{\partial t} + \frac{1}{2} \nabla |u_\alpha|^2 + g \nabla \eta + z_\alpha \left\{ \frac{1}{2} z_\alpha \nabla \left(\nabla \cdot \frac{\partial u_\alpha}{\partial t} \right) + \nabla \left(\nabla \cdot \left(h \frac{\partial u_\alpha}{\partial t} \right) \right) \right\} \\ + \nabla \left\{ \frac{1}{2} (z_\alpha^2 - \eta^2) (u_\alpha \cdot \nabla) (\nabla \cdot u_\alpha) + \frac{1}{2} [\nabla \cdot (hu_\alpha) + \eta \nabla \cdot u_\alpha]^2 \right\} \\ + \nabla \left\{ (z_\alpha - \eta) (u_\alpha \cdot \nabla) (\nabla \cdot (hu_\alpha)) - \eta \left[\frac{1}{2} \eta \nabla \cdot \frac{\partial u_\alpha}{\partial t} + \nabla \cdot \left(h \frac{\partial u_\alpha}{\partial t} \right) \right] \right\} = 0 \end{aligned} \quad (14)$$

which can be extended to deeper waters thereby improving the dispersive behavior (Galan et al., 2012; Simarro et al., 2015). Several models have been developed based on these equations either in finite differences, finite elements or by finite volume providing accurate results in reproducing laboratory experiments.

Fig. 14.13 shows the time history comparison between numerical results and experimental data at different reported gages. The first section has been used as the control section, allowing to synchronize model and experimental time. As seen, these models capture very well the dispersion in the approaching zone as well as the nonlinear decomposition over the bar. However, as already stated, due to the computational cost in solving the equations, these models are still far too operative for large areas of the littoral and research is devoted in code optimization.

Waves and Remote Sensing

General properties

Waves are usually the first type of motion that one can see at the sea surface, and they appear in all remotely sensed data. In some cases, the direct wave influence can be averaged out of the signal. In other cases, there is a residual bias due to the presence of waves. This is the case in range measurements with altimeters (e.g., Minster et al., 1991), velocity measurement with Doppler systems (Chapron et al., 2005; Nouguier et al., 2018), and surface brightness temperature measurements used to infer sea surface temperature or salinity (Reul and Chapron, 2003). Wave shapes and motion also introduce a variance in the measured quantity that can be useful in the case of sea level measurement with altimetry or can blur the signal beyond recognition in SAR imagery or interferometry (Peral et al., 2015).

All these effects are opportunities for measuring wave parameters or other processes thanks to their influence on waves. In the case when the source of light or radar transmitter is at the same location as the receptor (this is called monostatic geometry), radar waves reflected off from the sea surface is determined by either the variance of the surface slopes (usually called mean square slope or mss), when the source shines within about 20° of the vertical, or the wave spectral level at twice the horizontal radar wavelength for more oblique angles.

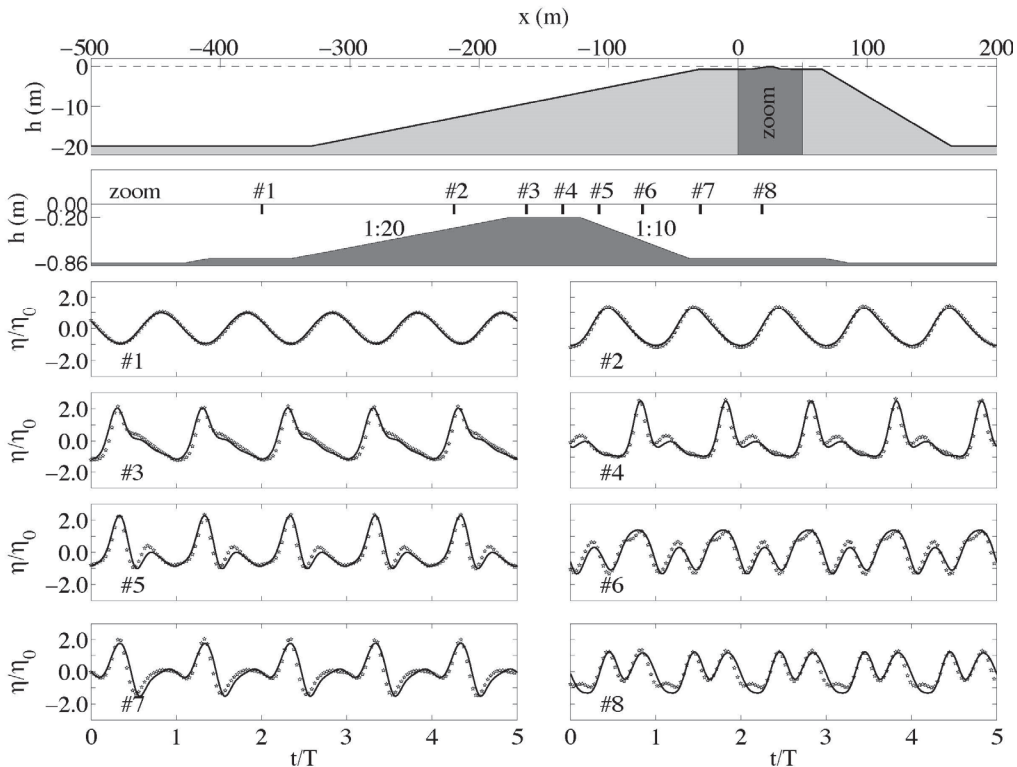


Figure 14.13. Evolution of the free surface at the different gages for the numerical results (solid lines) and experimental data (stars) from Dingemans (1994).

For near-vertical angles, the power recorded on a radar is well described by the theory for a nearly Gaussian distribution of surface slopes completely determined by the mss. In general, the mss is largely determined by the wind speed, but it is also modified by the stage of development of the wave field, increasing for more mature waves that generally correspond to higher wave heights, as shown in Fig. 14.14. A flat surface gives a strong return near zero incidence (vertical sounding) and the return power decreases as $1/\text{mss}$. For incidence angles larger than about 10° in Ku-band, the return increases with the roughness. Hence, the contrast in the sun reflection in an optical or radar image depends on the incidence; near the vertical a slick flat surface will appear bright, but it will be dark at higher incidences.

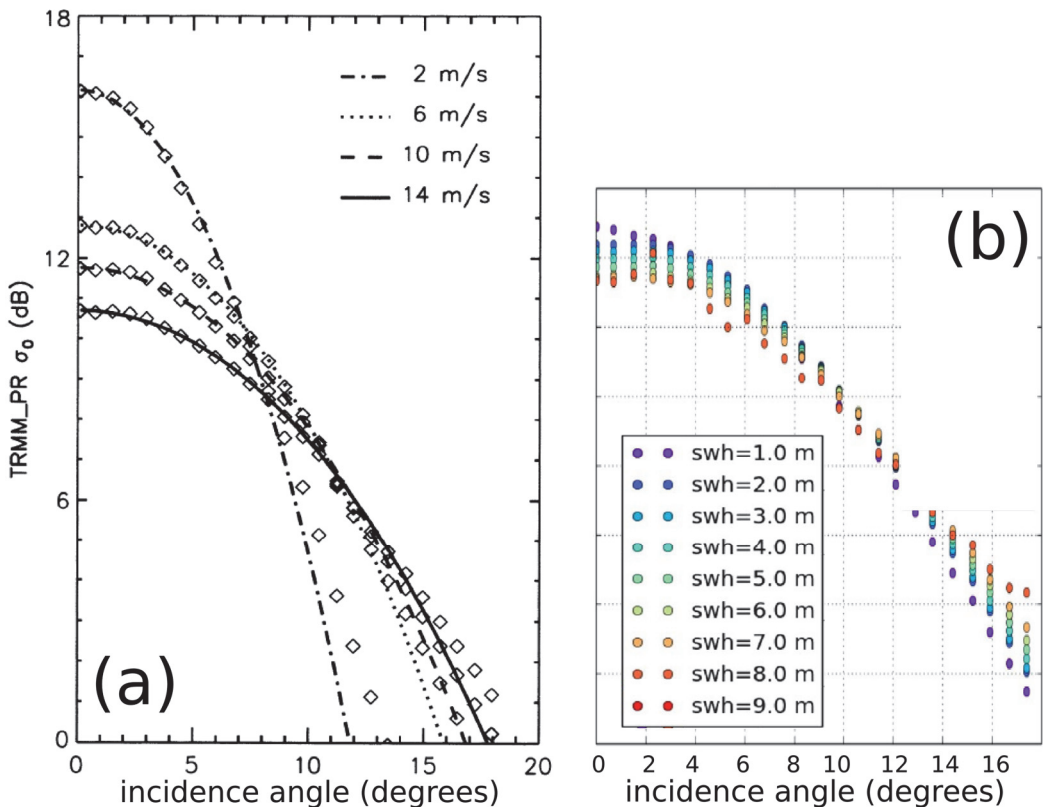


Figure 14.14. (a) Average backscatter power from the TRMM radar (from Freilich and Vanhoff, 2003). (b) Same variation for a given wind speed, as a function of wave height (from Nougquier et al., 2016).

Currents and waves in high-resolution optical imagery

The presence of currents and internal waves generally changes the amplitude of the waves, hence the mss, giving beautiful patterns in optical or SAR imagery, as illustrated in Fig. 14.15. The wind waves with wavelengths longer than a few meters also tilt the shorter waves and change the brightness. These properties can be exploited quantitatively to measure current gradients (Kudryavtsev et al., 2012; Rasclé et al., 2016, 2017), or waves (Kudryavtsev et al., 2017). Also, on Sentinel-2 and other similar sensors, the different color channels are not acquired simultaneously,

but with a time difference of the order of 1 s. This delay is enough to see the waves move between the different colors. From this motion, the dispersion of the waves given by Eq. 2 can be inverted to get a current velocity vector (Kudryavtsev et al., 2017), as illustrated in Fig. 14.16.

Sentinel 2, with a high resolution and large images that lead to relatively short revisit times, brings a revolution and amazing pictures that can be turned into hard numbers. Unfortunately, it is night half of the day on average and there can be many clouds. For these reasons, a routine monitoring of currents and waves is still more easily done with active radar systems.

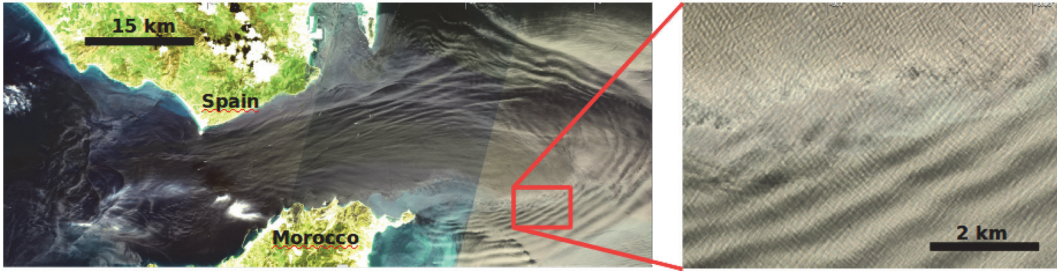


Figure 14.15. Example of a Sentinel-2 image acquired over the Straits of Gibraltar, 7 April 2016, see <http://bit.ly/1SN401K> for an interactive view.

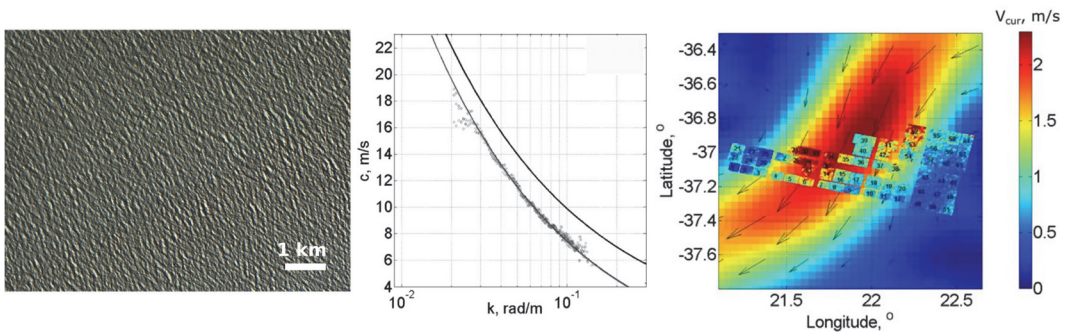


Figure 14.16. Analysis of surface current from a Sentinel-2 image over the Agulhas current (<https://odl.bzh/YqP5bd6P>). The left panel shows the wave pattern in the current, the middle shows the phase speed of the waves as a function of their wavenumber k with data available for wavelengths 50 to 300 m, and different symbols for different wave propagation direction. The upper curve is the dispersion without current $C = g/k$, the lower curve corresponds to $C = C + U$ with a current velocity $U = 2.2 \text{ m s}^{-1}$. The right panel shows the result of this analysis all across the image in small windows, with a background velocity given by satellite altimetry.

Current and waves with radars

Besides the satellite altimeters that provide estimates of H_s and mss that we will not discuss here (e.g., Gower, 1979; Quartly, 2000; Queffeulou, 2004; Ardhuin et al., 2010), more information on waves can be obtained from SARs. Unfortunately, for most applications, SAR images are not like photographs; the positions of pixels in a SAR image are displaced in the azimuth direction (the direction of the satellite motion) according to the relative velocity of the target and the solid Earth along the radar line of sight. This is very useful for measuring waves under sea ice (Ardhuin et al., 2017a) where the wave-induced velocities are small, but it leads to a strong blurring of the image

in the open ocean as soon as there are short energetic waves (Kerbaol et al., 1998; Stopa et al., 2015). For example, a typical vertical velocity fluctuation of 1m/s leads to a blurring on a scale of 200 m. As a result, in strong wind conditions SAR can only see waves travelling in the range direction, and very high resolution is useless for all other directions. This is illustrated with two SAR scenes in Fig. 14.17.

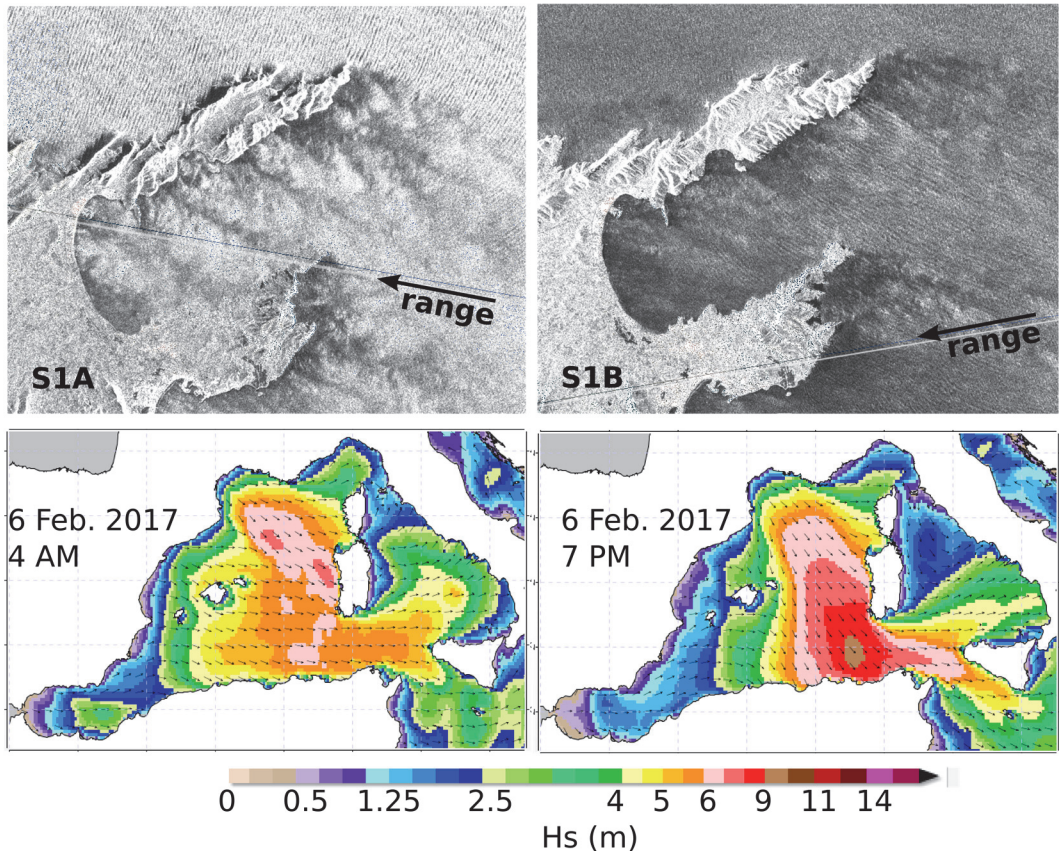


Figure 14.17. Example of waves seen by Sentinel 1A at 5:50 UTC (<https://odl.bzh/z3nM6X0E>) and 1B at 17:45 UTC during a severe Mediterranean storm on 6 February 2017. Top panels show the bay of Pollença, Mallorca, Spain. Range is the direction towards which the radar is pointing. The bottom panel shows model forecast wave height and directions from <http://marc.ifremer.fr/>.

The wind is very strong in the morning at 20 m/s and drops to 10 m/s in the evening. Strong winds, over 30 m/s, are also present off Cape Begur to the north, sending swells towards Mallorca. Waves at the northern tip of Mallorca in the morning are in the range direction of the S1A pass and thus very well-observed. However, there are also waves refracted into the Bay of Pollença (Mallorca, Spain), but they travel at an oblique direction and thus are blurred in the SAR image. In the evening, the dominant wave direction has turned to the north-west; they are invisible in the S1B pass, but we can see waves propagating into the bay as if they were coming out of nowhere. The alternative for measuring the directional wave spectrum is to use a rotating radar beam and not use synthetic aperture processing. This is the principle of the SWIM (Surface Waves Investigation and Monitoring) instrument that will be flown on CFOSAT, due for launch in 2018 (Hauser et al., 2017).

Current airborne and space-based measurements of surface velocity have been performed with across-track interferometric (ATI) SARs using two antennas (Goldstein and Zebker, 1987), giving a surface velocity projected on the satellite range direction. This has been generalized to squinted ATI SARs in order to provide the two components of the current vector (Buck, 2005; Wollstadt et al., 2016). More recently, Chapron et al. (2005) showed the potential of using the Doppler centroid of ocean backscatter received by a single antenna, as illustrated in Fig. 14.18.

Although this measurement is noisier than ATI resulting in an effective coarser resolution, the velocity given by the Doppler centroid is equivalent to an ATI measurement (Romeiser et al., 2013). Hence, the Doppler centroid method is a cost-effective solution for deriving current information from existing satellite missions such as Envisat and the Sentinel 1 constellation. This has already led to scientific application on the monitoring of intense currents (Rouault et al., 2010).

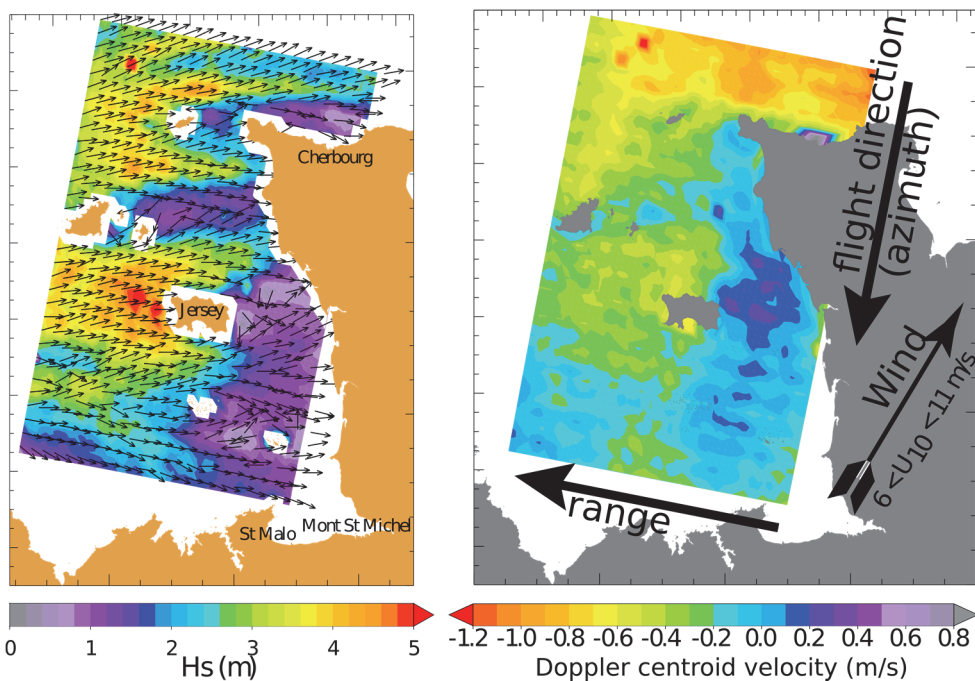


Figure 14.18. One of the first SAR images processed into a map of wave spectra giving wave heights (left) and Doppler centroid velocity (right). This was acquired by Envisat over Normandy on 10 March 2003 (Chapron et al., 2005; Arduin et al., 2012).

A dedicated mission that would measure surface current vector and waves based on Doppler centroid and a rotating real aperture radar has been preselected to be the ninth ESA Earth Explorer mission (Arduin et al., 2018). This Sea surface KInematics Multiscale monitoring (SKIM) mission would use the measurement of waves to correct for the large wave-induced bias in surface velocity that is measured in ATI or Doppler centroids. Existing European radar technology allows the use of a conical scanning radar beam over 12° of incidence, giving a typical swath width of 300 km. A preliminary error budget on this concept gives an effective resolution of surface currents with 60 km wavelength. Combined with the shorter revisit time, this is a very attractive alternative or

complement to measurements based on surface height with SWOT that have a narrow swath and only measure geostrophic currents, as shown on Fig. 14.19.

The proposed instrument can reveal features on tropical ocean and marginal ice zone dynamics that are inaccessible to other measurement systems, as well as a global monitoring of the ocean mesoscale that surpasses the capability of today's nadir altimeters. Measuring ocean wave properties facilitates many applications, from wave-current interactions and air-sea fluxes to the transport and convergence of marine plastic debris and assessment of marine and coastal hazards.

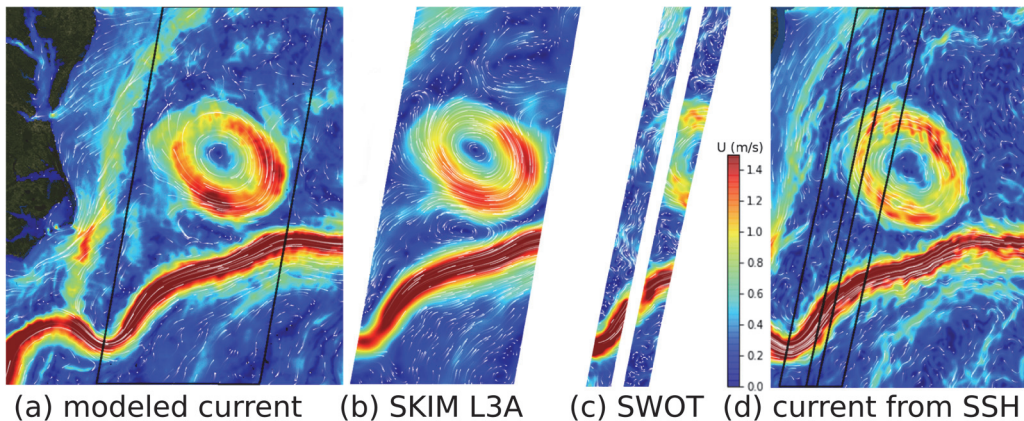


Figure 14.19. Simulated ocean currents over the Gulf Stream, and associated SKIM and SWOT simulated observations for a single satellite pass.

Acknowledgments

This work was supported by FP7-ERC grant « IOWAGA », EU-FP7 project SWARP, ONR grant number N0001416WX01117, and CNES. Visualization and analysis was greatly facilitated by the Syntool portal developed by OceanDataLab: <https://swarp.oceandatalab.com>. Support from LabexMer via grant ANR-10-LABX-19-01, and Copernicus Marine Environment Monitoring Service (CMEMS) as part of the Service Evolution program is gratefully acknowledged.

References

- Agnon, Y. 1999. Linear and nonlinear refraction and Bragg scattering of water waves. *Physical Review E*, 59, R1319–R1322.
- Agrawal, Y. C., Terray, E. A., Donelan, M. A., Hwang, P. A., Williams, A. J., Drennan, W., Kahma, K., and Kitaigorodskii, S. 1992. Enhanced dissipation of kinetic energy beneath breaking waves. *Nature*, 359, 219–220.
- Algué, J. 1900. Relation entre quelques mouvements microséismiques et l'existence, la position et la distance des cyclones à Manille (Philippines). Pages 131–136 of: *Congrès international de Météorologie*, Paris.
- Arduin, F. 2018. Ocean waves in geosciences. doi:10.13140/RG.2.2.16019.78888/2
- Arduin, F., Jenkins, A. D., Hauser, D., Reniers, A., and Chapron, B. 2005. Waves and operational oceanography: towards a coherent description of the upper ocean for applications. *Eos Trans. AGU*, 86(4), 37–39.
- Arduin, F., Chapron, B., and Collard, F. 2009. Observation of swell dissipation across oceans. *Geophys. Res. Lett.*, 36, L06607. doi:10.1029/2008GL037030.
- Arduin, F., Rogers, E., Babanin, A., Filipot, J.-F., Magne, R., Roland, A., van der Westhuysen, A., Queffelec, P., Lefevre, J.-M., Aouf, L., and Collard, F. 2010. Semi-empirical dissipation source functions for wind-wave models: part I, definition, calibration and validation. *J. Phys. Oceanogr.*, 40(9), 1917–1941.
- Arduin, F., Stutzmann, E., Schimmel, M., and Mangeney, A. 2011. Ocean wave sources of seismic noise. *J. Geophys. Res.*, 116, C09004. doi:10.1029/2011JC006952.

- Ardhuin, F., Balanche, A., Stutzmann, E., and Obrebski, M. 2012. From seismic noise to ocean wave parameters: general methods and validation. *J. Geophys. Res.*, 117, C05002. doi:10.1029/2011JC007449.
- Ardhuin, F., Rawat, A., and Aucan, J. 2014. A numerical model for free infragravity waves: Definition and validation at regional and global scales. *Ocean Modelling*, 77, 20–32.
- Ardhuin, F., Gualtieri, L., and Stutzmann, E. 2015. How ocean waves rock the Earth: two mechanisms explain seismic noise with periods 3 to 300 s. *Geophys. Res. Lett.*, 42, 765–772. doi:10.1002/2014GL062782.
- Ardhuin, F., Sutherland, P., Doble, M., and Wadhams, P. 2016. Ocean waves across the Arctic: attenuation due to dissipation dominates over scattering for periods longer than 19 s. *Geophys. Res. Lett.*, 43, 5775–5783. doi:10.1002/2016GL068204.
- Ardhuin, F., Chapron, B., Collard, F., Smith, M., Stopa, J., Thomson, J., Doble, M., Wadhams, P., Blomquist, B., Persson, O., and Collins, III, C. O. 2017a. Measuring ocean waves in sea ice using SAR imagery: A quasi-deterministic approach evaluated with Sentinel-1 and in situ data. *Remote sensing of Environment*, 189, 211–222. doi:10.1016/j.rse.2016.11.024.
- Ardhuin, F., Rasclé, N., Chapron, B., Gula, J., Molemaker, J., Gille, S. T., Menemenlis, D., and Rocha, C. 2017b. Small scale currents have large effects on wind wave heights. *J. Geophys. Res.*, 122(C6), 4500–4517. doi:10.1002/2016JC012413
- Ardhuin, F., Aksenov, Y., Benetazzo, A., Bertino, L., Brandt, P., Caubet, E., Chapron, B., Collard, F., Cravatte, S., Delouis, J.-M., Dias, F., Dibarboure, G., Gaultier, L., Johannessen, J., Korosov, A., Manucharyan, G., Menemenlis, D., Menendez, M., Monnier, G., Mouche, A., Noguier, F., Nurser, G., Rampal, P., Reniers, A., Rodriguez, E., Stopa, J., Tison, C., Ubelmann, C., van Sebille, E., and Xie, J. 2018. Measuring currents, ice drift, and waves from space: The sea surface kinematics multiscale monitoring concept, *Ocean Sci.*, 14, 337-354, <https://doi.org/10.5194/os-14-337-2018>, 2018
- Barber, N. F., Ursell, F., Darbyshire, J., and Tucker, M. J. 1946. A frequency analyser used in the study of ocean waves. *Nature*, 329–335.
- Bates, C. C. 1949. Utilization of wave forecasting in the invasions of Normandy, Burma, and Japan. *Ann. N. Y. Acad. Sci.*, 545–572.
- Beji, S., and K. Nadaoka. 1996. A formal derivation and numerical modelling of the improved Boussinesq equations for varying depth. *Ocean Engineering*, 23, 691–704.
- Benetazzo, A. 2006. Measurements of short water waves using stereo matched image sequences. *Coastal Eng.*, 53, 1013–1032.
- Berkhoff, J. C. W. 1972. Computation of combined refraction-diffraction. Pages 796–814 of: *Proceedings of the 13th International Conference on Coastal Engineering*, Vancouver. ASCE, New York, N. Y.
- Bernard, P. 1990. Historical sketch of microseisms from past to future. *Phys. Earth Planetary Interiors*, 63, 145–150.
- Bidlot et al., J.R., et al. 2007. Inter-comparison of Operational Wave Forecasting Systems, *Proceedings of the 10th wave hindcasting and forecasting workshop*, Oahu, Hawaii.
- Bidlot, J.R. 2017. Twenty-one years of wave forecast verification. *ECMWF Newsletter No. 150*, doi:10.21957/t4znuhb842
- Boccotti, P. 2000. *Wave mechanics for ocean engineering*. Amsterdam: Elsevier.
- Boussinesq, J. 1872. Théorie des ondes et des remous qui se propagent le long d'un canal rectangulaire horizontal, en communiquant au liquide contenu dans ce canal des vitesses sensiblement pareilles de la surface au fond. *J. Math. Pures Appl.*, 17(2), 55–108.
- Bromirski, P. D., Sergienko, O. V., and MacAyeal, D. R. 2010. Transoceanic infragravity waves impacting Antarctic ice shelves. *Geophys. Res. Lett.*, 37, L02502. doi:10.1029/2009GL041488.
- Buck, C. 2005. An extension to the wide swath ocean altimeter concept. Pages 543–5439 of: *Proceedings of the IEEE International Geoscience and Remote Sensing Symposium (IGARSS), 2013.*, vol. 8. IEEE. doi:10.1109/IGARSS.2005.1525970.
- Cavanié, A., Arhan, M., and Ezraty, R. 1976. A statistical relationship between individual heights and periods of storm waves. Pages 354–360 of: *Conference on the Behaviour of Off-Shore Structures (BOSS)*. The Norwegian Institute of Technology.
- Chapron, B., Collard, F., and Ardhuin, F. 2005. Direct measurements of ocean surface velocity from space: interpretation and validation. *J. Geophys. Res.*, 110(C07008). doi:10.1029/2004JC002809.
- Cox, C., and Munk, W. 1954. Measurement of the roughness of the sea surface from photographs of the sun's glitter. *J. Opt. Soc. Am.*, 44(11), 838–850.
- D'Asaro, E. A. 2014. Turbulence in the Upper-Ocean Mixed Layer. *Annu. Rev. Mar. Sci.*, 6, 101–115. doi:10.1146/annurev-marine-010213-135138.
- de Laplace, P. S. 1776. Suite des recherches sur plusieurs points du système du monde (XXV–XXVII). *Mém. Présentés Acad. R. Sci. Inst. France*, 542–552.

- de Saint-Venant, A. J. C. B., and Flamant, A. 1888. De la houle et du clapotis. *Annales des Ponts et Chaussées*, 6, 705–773.
- Dean, R. G., and Dalrymple, R. A. 1984. *Water wave mechanics for engineers and scientists*. Englewood Cliffs, New Jersey 07632: Prentice-Hall, Inc.
- Deane, G. B., and Stokes, M. D. 2002. Scale dependence of bubble creation mechanisms in breaking waves. *Nature*, 418, 839–844.
- Dingemans, M. W. 1994. Comparison of computations with Boussinesq-like models and laboratory measurements. Mast-G8M technical report, Delft Hydraulics, Delft, The Netherlands.
- Dingemans, M. W. 1997. *Water wave propagation over uneven bottoms. Part 1 linear wave propagation*. Singapore: World Scientific. 471 p.
- Eckart, C. 1952. The propagation of gravity waves from deep to shallow waters. *National Bureau of Standards*, 20.
- Elfouhaily, T., Chapron, B., Katsaros, K., and Vandemark, D. 1997. A unified directional spectrum for long and short wind-driven waves. *J. Geophys. Res.*, 102(C7), 15781–15796.
- Freilich, M. H., and Vanhoff, B. A. 2003. The Relationship between Winds, Surface Roughness, and Radar Backscatter at Low Incidence Angles from TRMM Precipitation Radar Measurements. *J. Atmos. Ocean Technol.*, 20, 549–562.
- Gain, L. 1918. La prédiction des houles au Maroc. *Annales Hydrographiques*, 65–75.
- Galan, A., G., Orfila, A., Simarro, J., and Liu, P. L.-F. 2012. Fully Nonlinear Model for Water Wave Propagation from Deep to Shallow Waters. *Journal of Waterway, Port, Coastal, and Ocean Engineering*, 138(5), 362–371.
- Gelci, R., Cazalé, H., and Vassal, J. 1957. Prédiction de la houle. La méthode des densités spectroangulaires. *Bulletin d'information du Comité d'Océanographie et d'Etude des Côtes*, 9, 416–435.
- Gobbi, M. F., Kirby, J. T., and Wei, G. 2000. A fully nonlinear Boussinesq model for surface waves: part II. Extension to $O(kh)^4$. *Journal of Fluid Mechanics*, 405, 182–210.
- Goldstein, R. M., and Zebker, H. A. 1987. Interferometric radar measurement of ocean surface current. *Nature*, 328, 707–709.
- Gourrion, J., Vandemark, D., Bailey, S., and Chapron, B. 2002. Investigation of C-band altimeter cross section dependence on wind speed and sea state. *Can. J. Remote Sensing*, 28(3), 484–489.
- Gower, J. F. R. 1979. The computation of ocean wave heights from GEOS-3 satellite radar altimeter. *Remote sensing of Environment*, 8, 97–114.
- Green, A. E., and Naghdi, P. M. 1976. A derivation of equations for wave propagation in water of variable depth. *Journal of Fluid Mechanics*, 78, 237–246.
- Grevemeyer, I., Herber, R., and Essen, H.-H. 2000. Microseismological evidence for a changing wave climate in the northeast Atlantic Ocean. *Nature*, 408, 349–351.
- Hanafin, J., Quilfen, Y., Ardhuin, F., Sienkiewicz, J., Queffeuilou, P., Obrebski, M., Chapron, B., Reul, N., Collard, F., Corman, D., de Azevedo, E. B., Vandemark, D., and Stutzmann, E. 2012. Phenomenal sea states and swell radiation: a comprehensive analysis of the 12-16 February 2011 North Atlantic storms. *Bull. Amer. Meteorol. Soc.*, 93, 1825–1832. doi:10.1175/BAMS-D-11-00128.1.
- Hasselmann, K. 1962. On the non-linear energy transfer in a gravity wave spectrum, part 1: general theory. *J. Fluid Mech.*, 12, 481–501.
- Hasselmann, K. 1963. A statistical analysis of the generation of microseisms. *Rev. of Geophys.*, 1(2), 177–210.
- Hasselmann, K., Barnett, T. P., Bouws, E., Carlson, H., Cartwright, D. E., Enke, K., Ewing, J. A., Gienapp, H., Hasselmann, D. E., Kruseman, P., Meerburg, A., Müller, P., Olbers, D. J., Richter, K., Sell, W., and Walden, H. 1973. Measurements of wind-wave growth and swell decay during the Joint North Sea Wave Project. *Deut. Hydrogr. Z.*, 8(12), 1–95. Suppl. A.
- Hasselmann, S., Hasselmann, K., Allender, J., and Barnett, T. 1985. Computation and parameterizations of the nonlinear energy transfer in a gravity-wave spectrum. Part II: Parameterizations of the nonlinear energy transfer for application in wave models. *J. Phys. Oceanogr.*, 15, 1378–1391.
- Hasselmann, K., Chapron, B., Aouf, L., Ardhuin, F., Collard, F., Engen, G., Hasselmann, S. and Heimbach, P., Janssen, P., Johnsen, H., Krogstad, H., Lehner, Susanne, Li, J.-G., Li, Xiao-Ming, Rosenthal, W. and Schulz-Stellenfleth, J. (2012) *The ERS SAR Wave Mode – A Breakthrough in global ocean wave observations*. In: *ERS Missions - 20 Years of Observing Earth* ESA Scientific Publications, SP-1326. ESA. pp. 1-38.
- Hauser, D., Tison, C., Amiot, T., Delaye, L., Corcoral, N., and Castillan, P. 2017. SWIM: The First Spaceborne Wave Scatterometer. *IEEE Trans. on Geosci. and Remote Sensing*, 55(5), 3000–3014.
- Herbers, T. H. C., and Burton, M. C. 1997. Nonlinear shoaling of directionally spread waves on a beach. *J. Geophys. Res.*, 102(C9), 21,101–21,114.

- Hersbach, H., 2010. Assimilation of scatterometer data as equivalent-neutral wind, Technical Memorandum 629, ECMWF.
- Iribarren, R., and Nogales, C. 1949. Protection des ports. Pages 31–80 of: Proceedings XVIIth International Navigation Congress, Section II, Communication, 4, Lisbon.
- Janssen, P. A. E. M. 1989. Wave-induced stress and the drag of air flow over sea waves. *J. Phys. Oceanogr.*, 19, 745–754.
- Janssen, P. 2004. The interaction of ocean waves and wind. Cambridge: Cambridge University Press.
- Janssen, P., Doyle, J.-D., Bidlot, J., Hansen, B., Isaksen, L., and Viterbo, P. 2001. Impact and feedback of ocean waves on the atmosphere. Tech. rept. Memorandum 341. Research Department, ECMWF, Reading, U. K.
- Janssen, P. A. E. M. 2008. Progress in ocean wave forecasting. *J. Comp. Phys.*, 227, 3572–3594. doi:10.1016/j.jcp.2007.04.029.
- Jarosz, E., Mitchell, D. A., Wang, D. W., and Teague, W. J. 2007. Bottom-up determination of air-sea momentum exchange under a major tropical cyclone. *Science*, 315, 1707–1709.
- Kerbaol, V., Chapron, B., and Vachon, P. 1998. Analysis of ERS-1/2 synthetic aperture radar wave mode images. *J. Geophys. Res.*, 103(C4), 7833–7846.
- Kirby, J. T., and Dalrymple, R. A. 1983. Propagation of obliquely incident water waves over a trench. *J. Fluid Mech.*, 133, 47–63.
- Kudryavtsev, V., Yurovskaya, M., Chapron, B., Collard, F., and Donlon, C. 2017. Sun glitter Imagery of Surface Waves. Part 1: Directional spectrum retrieval and validation. *J. Geophys. Res.*, 122. doi:10.1002/2016JC012425.
- Kudryavtsev, V., Myasoedov, A., Chapron, B., Johannessen, J. A., and Collard, F. 2012. Imaging mesoscale upper ocean dynamics using synthetic aperture radar and optical data. *J. Geophys. Res.*, 117, C04029. doi:10.1029/2011JC007492.
- Kukulka, T., Plueddemann, A. J., Trowbridge, J. H., and Sullivan, P. P. 2009. Significance of Langmuir circulation in upper ocean mixing: Comparison of observations and simulations. *Geophys. Res. Lett.*, 36, L10603. doi:10.1029/2009GL037620.
- Lavrenov, I. V. 2003. Wind-waves in oceans: dynamics and numerical simulations. Berlin: Springer.
- Leckler, F., Ardhuin, F., Peureux, C., Benetazzo, A., Bergamasco, F., and Dulov, V. 2015. Analysis and interpretation of frequency-wavenumber spectra of young wind waves. *J. Phys. Oceanogr.*, 45, 2484–2496. doi:10.1175/JPO-D-14-0237.1.
- Lefèvre, J.-M., and Aouf, L. (2012) Latest developments in wave data assimilation, proceedings of the ECMWF workshop on ocean waves.
- Lionello, P., Günther, H, and Janssen, PAEM, 1992. Assimilation of altimeter data in a global third generation wave model. *J. Geophys. Res.*, 97(C9): 14,453-14,474.
- Liu, P. L.-F., and Losada, I. 2002. Wave propagation modeling in coastal engineering. *Journal of Hydraulic Research*, 40, 229–240.
- Liu, P. L.-F., and Orfila, A. 2004. Viscous effects on transient long-wave propagation. *Journal of Fluid Mechanics*, 520, 83–92.
- Liu, P.-F., Simarro, G., Vandever, J., and Orfila, A. 2006. Experimental and numerical investigation of viscous effects on solitary wave propagation in a wave tank. *Coastal Engineering*, 53(2), 181–190.
- Longuet-Higgins, M. S. 1950. A theory of the origin of microseisms. *Phil. Trans. Roy. Soc. London A*, 243, 1–35.
- Longuet-Higgins, M. S., and Stewart, R. W. 1962. Radiation stresses and mass transport in surface gravity waves with application to ‘surf beats’. *J. Fluid Mech.*, 13, 481–504.
- Lynett, P., and Liu, P. L.-F. 2002. A two layer approach to wave modeling. *The Royal Society London, A*, 46(2), 89–107.
- Madsen, P. A., and Schaffer, H. A. 1998. Higher-order Boussinesq-type equations for surface gravity waves: derivation and analysis. *Phil. Trans. Royal Society of London A*, 356, 3123–3184.
- Madsen, P. A., and Sorensen, O. R. 1992. A new form of the Boussinesq equations with improved linear dispersion characteristics. Part 2: A slowly-varying bathymetry. *Coastal Engineering*, 18, 183–204.
- Mastenbroek, C., Burgers, G., and Janssen, P. A. E. M. 1993. The dynamical coupling of a wave model and a storm surge model through the atmospheric boundary layer. *J. Phys. Oceanogr.*, 23, 1856–1867.
- Mei, C. C. 1989. Applied dynamics of ocean surface waves. Second Edn. Singapore: World Scientific. 740 p.
- Miche, A. 1944. Mouvements ondulatoires de la mer en profondeur croissante ou décroissante. Forme limite de la houle lors de son déferlement. Application aux digues maritimes. Deuxième partie. Mouvements ondulatoires périodiques en profondeur régulièrement décroissante. *Annales des Ponts et Chaussées, Tome 114*, 131–164, 270–292.

- Minster, J. F., Jourdan, D., Boissier, C., and Midol-Monnet, P. 1991. Estimation of the Sea-state bias in radar altimeter Geosat data from examination of frontal systems. *J. Atmos. Ocean Technol.*, 9, 174–187.
- Montagne, R. 1922. Le service de prédiction de la houle au Maroc. *Annales Hydrographiques*, 157–186.
- Munk, W. H. 1950. Origin and generation of waves. Pages 1–4 of: *Proceedings 1st International Conference on Coastal Engineering*, Long Beach, California. ASCE.
- Nouguier, F., Mouche, A., Rascle, N., Chapron, B., and Vandemark, D. 2016. Analysis of Dual-Frequency Ocean Backscatter Measurements at Ku- and Ka-Bands Using Near-Nadir Incidence GPM Radar Data. *IEEE Geoscience and Remote Sensing Letters*, 31, 2023–2245. doi:10.1109/LGRS.2016.2583198.
- Nouguier, F., Chapron, B., Collard, F., Mouche, A., Rascle, N., Ardhuin, F., and Wu, X. 2018. Sea surface kinematics from near-nadir radar measurements. *IEEE Trans. on Geosci. and Remote Sensing*, in press.
- Nwogu, O. 1993. Alternative form of Boussinesq equations for nearshore wave propagation. *Journal of Waterway, Port, Coastal and Ocean Engineering*, 119(6), 618–638.
- Orfila, A., Simarro, G., and Liu, P. 2007. Bottom friction and its effects on periodic long wave propagation. *Coastal Engineering*, 54(11), 856–864.
- Peral, E., Rodriguez, E., and Esteban-Fernandez, D. 2015. Impact of Surface Waves on SWOT's Projected Ocean Accuracy. *Remote Sensing*, 7(11), 14509–14529. doi:10.3390/rs71114509.
- Peregrine, D. H. 1967. Long waves on a beach. *J. Fluid Mech.*, 27, 815–827.
- Peureux, C., and Ardhuin, F. 2016. Ocean bottom pressure records from the Cascadia array and short surface gravity waves. *J. Geophys. Res.*, 121, 28622873. doi:10.1002/2015JC011580.
- Peureux, C., Benetazzo, A., and Ardhuin, F. 2017. Note on the directional properties of meter-scale gravity waves. *Ocean Science Discussions*.
- Phillips, O. M. 1977. *The dynamics of the upper ocean*. London: Cambridge University Press. 336 p.
- Pierson, Jr, W. J., and Moskowitz, L. 1964. A proposed spectral form for fully developed wind seas based on the similarity theory of S. A. Kitaigorodskii. *J. Geophys. Res.*, 69(24), 5,181–5,190.
- Pineau-Guillou, L., Ardhuin, F., Bouin, M.-N., Redelsperger, J.-L., Chapron, B., Bidlot, J., and Quilfen, Y. 2017. Strong winds in a coupled wave-atmosphere model during a North Atlantic storm event: evaluation against observations. *Quart. Journ. Roy. Meteorol. Soc.*, in press.
- Plant, W. J. 1982. A relationship between wind stress and wave slope. *J. Geophys. Res.*, 87, 1961–1967.
- Quartly, G. D. 2000. The Gate Dependence of Geophysical Retrievals from the TOPEX Altimeter. *J. Atmos. Ocean Technol.*, 17, 1247–1251.
- Queffelec, P. 2004. Long term validation of wave height measurements from altimeters. *Marine Geodesy*, 27, 495–510. DOI: 10.1080/01490410490883478.
- Rascle, N., and Ardhuin, F. 2013. A global wave parameter database for geophysical applications. Part 2: model validation with improved source term parameterization. *Ocean Modelling*, 70, 174–188. doi:10.1016/j.ocemod.2012.12.001.
- Rascle, N., Nouguier, F., Chapron, B., Mouche, A., and Ponte, A. 2016. Surface roughness changes by fine scale current gradients: Properties at multiple Wind waves azimuth view angles. *J. Phys. Oceanogr.*, 46, 3681–3694. doi:10.1175/JPO-D-15-0141.1.
- Rascle, N., Molemaker, J., Marié, L., Nouguier, F., Chapron, B., Lund, B., and Mouche, A. 2017. Intense deformation field at oceanic front inferred from directional sea surface roughness observations. *Geophys. Res. Lett.*, 48, 5599–5608. doi:10.1002/2017GL073473.
- Reniers, A. J. H. M., Roelvink, J. A., and Thornton, E. B. 2004. Morphodynamic modeling of an embayed beach under wave group forcing. *J. Geophys. Res.*, 109, C01030. doi:10.1029/2002JC001586.
- Reul, N., and Chapron, B. 2003. A model of sea-foam thickness distribution for passive microwave remote sensing applications. *J. Geophys. Res.*, 108(C10), 3321. doi:10.1029/2003JC001887.
- Rogers, W. E., Thomson, J., Shen, H. H., Doble, M. J., Wadhams, P., and Cheng, S. 2016. Dissipation of wind waves by pancake and frazil ice in the autumn Beaufort Sea. *J. Geophys. Res.*, 121. doi:10.1002/2016JC012251.
- Romeiser, R., Runge, H., Suchandt, S., Kahle, R., Rossi, C., and Bell, P. 2013. Comparison Of Current Fields From Terrasar-X And Tandem-X Along-Track Interferometry And Doppler Centroid Analysis. In: *Proceedings of the IEEE International Geoscience and Remote Sensing Symposium (IGARSS)*, 2013. IEEE.
- Rouault, M. J., Mouche, A., Collard, F., Johannessen, J. A., and Chapron, B. 2010. Mapping the Agulhas Current from space: An assessment of ASAR surface current velocities. *J. Geophys. Res.*, 41, C10026. doi:10.1029/2009JC006050.
- Schaffer, H. A. 1996. Second order wavemaker theory for irregular waves. *Ocean Engineering*, 23, 47–88.

- Sepulveda, H. H., Queffeuou, P., and Ardhuin, F. 2015. Assessment of SARAL AltiKa wave height measurements relative to buoy, Jason-2 and Cryosat-2 data. *Marine Geodesy*, 38(S1), 449–465. doi:10.1080/01490419.2014.1000470.
- Serre, F. 1953. Contribution à l'étude des écoulements permanents et variables dans les canaux. *Houille Blanche*, 8, 830–872.
- Shapiro, N. M., Campillo, M., Stehly, L., and Ritzwoller, M. H. 2005. High-Resolution Surface-Wave Tomography from Ambient Seismic Noise. *Science*, 307, 1615–1617. doi:10.1111/j.1365-246X.2006.03240.x.
- Shen, H. H., Ackley, S. F., and Hopkins, M. A. 2001. A conceptual model for pancake ice formation in a wave field. *Annales Geophysicae*, 33(C1), 361–367. doi:10.3189/172756401781818239.
- Sheremet, A., Staples, T., Ardhuin, F., Suanez, S., and Fichaut, B. 2014. Observations of large infragravity-wave run-up at Banneg Island, France. *Geophys. Res. Lett.*, 41.
- Simarro, G., Orfila, A., Mozos, C. M., and Pruneda, R. E. On the linear stability of one- and two-layer Boussinesq-type equations for wave propagation over uneven beds.
- Smith, R., and Sprinks, T. 1975. Scattering of surface waves by a conical island. *J. Fluid Mech.*, 72, 373.
- Soloviev, A. V., Lukas, R., Donelan, M. A., Haus, B. K., and Ginis, I. 2014. The air-sea interface and surface stress under tropical cyclones. *Scientific Reports*, 4, 5306. doi:10.1038/srep05306.
- Stockdon, H. F., Holman, R. A., Howd, P. A., and Sallenger, Jr., A. H. 2006. Empirical parameterization of setup, swash, and runup. *Coastal Eng.*, 53, 573–588.
- Stopa, J.E., 2018. Wind forcing calibration and wave hindcast comparison using multiple reanalysis and merged satellite wind datasets. *Ocean Modelling*, in press.
- Stopa, J. E., Ardhuin, F., Chapron, B., and Collard, F. 2015. Estimating wave orbital velocity through the azimuth cutoff from space-borne satellite. *J. Geophys. Res.*, 130, 7616–7634. doi:10.1002/2015JC011275.
- Stopa, J. E., Ardhuin, F., Bababin, A., and Zieger, S. 2016. Comparison and validation of physical wave parameterizations in spectral wave models. *Ocean Modelling*, 103, 2–17. doi:10.1016/j.ocemod.2015.09.003.
- Sullivan, P. P., and McWilliams, J. C. 2010. Dynamics of Winds and Currents Coupled to Surface Waves. *Annu. Rev. Fluid Mech.*, 42, 19–42.
- Sverdrup, H. U., and Munk, W. H. 1947. Wind, sea, and swell: theory of relations for forecasting. Tech. rept. 601. U. S. Hydrographic Office.
- Tayfun, A. 1980. Narrow-band nonlinear sea waves. *J. Geophys. Res.*, 85(C3), 1543–1552.
- The WAVEWATCH III Development Group. 2016. User manual and system documentation of WAVEWATCH III version 5.16. Tech. Note 329. NOAA/NWS/NCEP/MMAB, College Park, MD, USA. 326 pp. + Appendices.
- Tolman, H. L. 1995. On the selection of propagation schemes for a spectral wind wave model. Office Note 411. NWS/NCEP. 30 pp + figures.
- Tolman, H. L. 2008. A mosaic approach to wind wave modeling. *Ocean Modelling*, 25, 35–47. doi:10.1016/j.ocemod.2008.06.005.
- Tsay, T.-K., and Liu, P. L.-F. 1982. Numerical solution of water-wave refraction and diffraction problems in the parabolic approximation. *Journal of Geophysical Research: Oceans*, 87(C10), 7932–7940.
- Wei, G., and Kirby, J. T. 1995. Time-dependent numerical code for extended Boussinesq equations. *Journal of Waterway, Port, Coastal and Ocean Engineering*, 121(5), 251–261.
- White, B. S., and Fornberg, B. 1998. On the chance of freak waves at sea. *J. Fluid Mech.*, 355, 113–138.
- Wollstadt, S., Lopez-Dekker, P., De Zan, F., and Younis, M. 2016. Design Principles and Considerations for Spaceborne ATI SAR-Based Observations of Ocean Surface Velocity Vectors. *IEEE Trans. on Geosci. and Remote Sensing*, 99, 1–20. doi:10.1109/TGRS.2017.2692880.
- Yueh, S. H., Tang, W., Fore, A. G., Neumann, G., Hayashi, A., Freedman, A., Chaubell, J., and Lagerloef, G. S. E. 2013. L-Band Passive and Active Microwave Geophysical Model Functions of Ocean Surface Winds and Applications to Aquarius Retrieval. *IEEE Trans. on Geosci. and Remote Sensing*, 51, 4619–4632.

